OSTBAYERISCHE TECHNISCHE HOCHSCHULE REGENSBURG

UNIVERSITAT POLITÈCNICA DE CATALUNYA BARCELONATECH
Escola d'Enginyeria de Barcelona Est

BACHELOR THESIS

Francesc Xavier Espinosa Vila

CFD SIMULATIONS OF AN ARCHIMEDES SCREW

Faculty:	Mechanical Engineering
Course of studies:	Mechanical Engineering
Deadline for submission:	30.06.2019
Supervisor:	Prof. Dr. Oliver Webel

Statement

1. I am aware that this copy of the bachelor thesis becomes the property of the Ostbayerische Technische Hoschschule Regensburg.
2. I hereby declare that I have written this bachelor thesis independently, have not yet submitted it for examination purposes elsewhere, have not used any sources and aids other than those stated, and have marked verbatim and meaningful quotations as such.

_____

Place, date and signature

Student:	Francesc Xavier Espinosa Vila
Matriculation number:	2927262
Processing time:	30.10.2018 – 30.06.2019

Abstract

As a consequence of global warming, new sources of renewable energy are becoming an increasing priority. Archimedes' screw generator allows to transform the potential energy of a fluid at a low-head hydraulic sites into mechanical energy as few generators have been able to do until now. Being a new technology, this thesis tries to provide a numerical research for the study of said screw turbine and extract results in the form of efficiency to be able to see the operation of this type of generator. The Navier-Stokes 3D equations are solved with the k-omega SST turbulence model. The geometry of the screw has been provided by an energy consultancy in Regensburg, Germany.

Table of contents

List of figures

List of tables

1. Preface

Nowadays, it is essential to be aware of how important the use of renewable energies is for our planet and life on it. Global warming is occurring that may be irreparable for life on earth. Glaciers are melting, sea levels are rising, forests are drying up and all this is caused and increased by so-called greenhouse gases caused by the combustion of fossil fuels. Apart from this, it is very important to find alternative energy sources to fossil fuels, since, by definition, fossil fuels are non-renewable energy sources, that is, with limited resources.

This is where the importance of renewable energies comes in. By definition, renewable energies are those whose source of resources is unlimited and comes from natural resources. These include wind energy, solar energy, geothermal energy, tidal energy, wave energy, biomass, biofuels and finally hydroelectric energy.

Hydraulic energy has been used for thousands of years. Historically, it was used to help in the work and movement of mechanical devices, such as mills or paddle wheels to help grind grain. It was not until the 19th century that we can start talking about hydroelectric power. That is when hydraulic energy begins to be used to generate electricity. The first hydroelectric plant was built in 1879 at Niagara Falls, but it would not start generating electricity until 1881.

One of the major problems with this type of renewable energy is the destruction of the aquatic ecosystem because it involves the construction of large reservoirs to control the flow of water through the turbines. This can also lead to the loss of fertile land and a drastic change in the flow of a river. In this thesis we will talk about a device that has existed for thousands of years, but has been reinvented to produce a more environmentally friendly type of hydropower.

2. Introduction

Germany is considered "the world's first major renewable energy economy" thanks to its production of wind, solar and biomass energy. Official statistics indicate that approximately 32% of the electricity consumed in Germany comes from renewable energy plants. The *Energiewende* (*Germany's Energy Transition Plan*) is to reach 80% electricity production from renewable sources by 2050. More than 23,000 wind turbines make Germany the third country in the world with the largest installed wind energy capacity, and it also ranks third in photovoltaic capacity with 1.4 million solar photovoltaic systems distributed throughout the country. On January 1 and May 1, 2018, power plants that produce energy from renewable resources in Germany produced more energy than was consumed nationwide for two and a half hours [1].

According to the IHA (*International Hydropower Association*), hydroelectric installations in Germany account for approximately 6% of the country's installed energy capacity, and about 3% of the net electricity generation [2]. The first Archimedean screw used as a turbine was installed in 1997 on the Eger River in Germany, since then more than 400 have been installed worldwide [3]. Currently, several new hydropower projects are under development, and were expected to come online in 2020.

The hydropower potential in Germany is considered to be practically exploited to its full potential. Now, it is time to exploit its full capacity, increasing the efficiency and development of existing plants, and try to do it in an environmentally friendly way. Therefore, it is necessary to research and develop new technologies, as is the case of the Archimedean screw used as a turbine.

This thesis will do CFD simulations of an Archimedean screw using Ansys Fluent software. The CAD geometry was provided by a local consultancy in Regensburg, Germany.

3. Archimedes screw

The invention of the screw is attributed to Archimedes of Syracuse (circa 287-212 BCE) but, according to many historians, the screw was created in Egypt before Archimedes was born, but it was he who adapted and popularized it to use the screw as a pump for irrigation.

An Archimedean screw consists of a helical blade that surrounds a hollow pipe, which through the rotation movement, is able to transport liquids or granulated materials. The Archimedean screw has two main variants: as a screw conveyor or as a screw turbine. It can also have many other functions, such as fish ladder, for land reclamation, injection moulding and even for the replacement of heart valves [4].

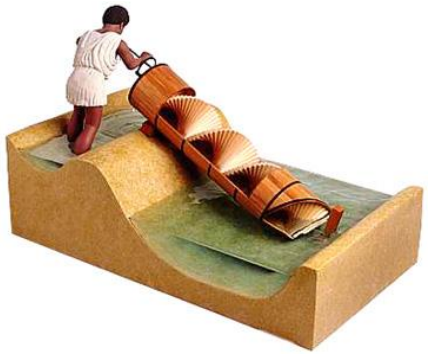

Figure 3.1 Screw used as a pump for irrigation [5]

3.1. Screw as a pump

As mentioned above, historically the screw conveyor was used for transporting water to irrigation systems or for dewatering low-lying areas. Today, the conveyor screw is mainly used to move granulated solid materials, such as cereal grains or animal feed, in an efficient and controlled manner, as the rate of material delivered is controlled by varying the rotation of the shaft.

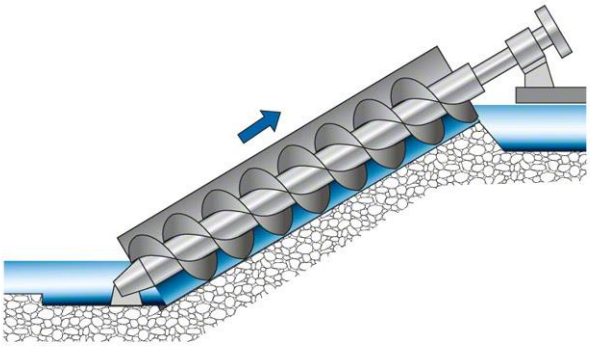

Figure 3.2 Archimedes screw as a pump [6]

Nowadays, one of the most important applications of the screw as a pump is the drainage of areas that are below sea level in order to be useful either for agriculture or construction. This application is widely used in Holland, as more than 20% of the country is below sea level and without constant drainage more than half the country would be completely flooded [7].

Another important utility for the screw as a pump is as a temporary replacement of a heart valve. Since the 1980s, Archimedes' screw has been used to simulate the process of the left ventricle to pump blood with constant flow. A single device can last about 10 years, giving the patient time to find a donor, although research is underway to make devices that can be permanent [4].

Another utility for the screw is a fish ladder, that is, to transport fish safely from one area to another. When a fish enters the screw, it remains in the same section of water from the time it enters until it exits the screw, which means that the life of the fish is not endangered at any time.

3.2. Screw as a turbine

The other main use of an Archimedean screw is reversed, as a screw turbine. The water is introduced through the upper part of the screw, and thanks to the energy it carries, it causes the screw to turn, thus turning it into a turbine, since the turn is used to drive an electric generator.

The Archimedes screw as a turbine has been implemented as a hydro turbine since Karl-August Radlik applied for its patent in 1991 [3]. The patent describes a screw pump, with either single or multiple blades, that sits at an inclined angle in a fixed trough, operating in reverse to generate hydroelectric energy from the difference in head between two water surfaces. This way of using the screw is going to be the object of study of this thesis.

Figure 3.3 Archimedes screw as a generator [8]

3.2.1. Advantages

Using the Archimedes screw as a turbine has many advantages over other hydroelectric generators and technologies.

One of the most important advantages is that it is environmentally friendly. In the same way the screw is used for fish ladder, screw turbines allows fish passage through the turbine itself. One of the reasons this happens is because of the low rotation velocities at which the screw works. This low rotation velocity causes shear stresses or pressure variations to be within the normal levels that fish must endure in natural environments. Another reason why the screw is not harmful to fish is that once the fish has entered the screw, it stays in the same section of water until it exits the screw, and that means that it does not have to swim through the blades of the screw and can get hurt badly.

Another advantage is that, in the same way that it allows fish to pass through, the screw also allows silt and debris to do it. That has many advantages. One of them is that it allows to regulate and control the silt of a river in which it is not possible to use conventional drainage methods, thus demonstrating its immunity against damage caused by sediments.

Another advantage related to debris is that, by allowing it to pass through, the screw will not get stuck as often, making the maintenance of the screw much lower than other hydroelectric generators.

Following the cost-related path, Archimedes screws are usually installed in old stations or dams and therefore civil construction costs are considered to be much lower than those of any other power generator. All this in addition to its simple design, which does not require expensive or complex parts, making the manufacturing costs are also low, as well as the costs of repairs and spare parts because as the speed of rotation is so low, there are many fewer cycles and therefore the parts will wear much less than in any other type of turbine.

The last main advantage of an ASG, is the reasonable large operational range it has [7]. The turbine has a wide range of flow rates and rotational speeds where it can operate with considerably higher efficiency compared to other hydroelectric generators. In addition to that, the screw can be installed in two different ways within a river. The main way is with an angle of inclination confined within a canal. This way is the most used since it operates in a flow and height range not covered by other conventional turbines, and with a higher efficiency than the water wheels, which seem to be the only viable alternative with these height and flow ranges.

The ASGs can also be installed horizontally or perpendicular to the river [9]. The screw is partially submerged into the river, with an angle of inclination equal to zero and without being confined within a trough, thus taking advantage of all the hydrokinetic energy carried by the river to transform it into energy. The design of these screws is slightly different from that of the inclined screws as these screws

are symmetrical in themselves, so that they could operate with the two directions of the river flow. They are designed to operate where the height of the river is very low and there are no changes in height. This type of installation is still being researched and studied as it is very recent, but it is still very promising.

Figure 3.4 Horizontal ASG [9]

3.2.2. Operating principle of an ASG

An Archimedes screw plant works as follows: water flows through the screw pushing it to turn, although it is the generator that forces the initial turn of the screw. The transmission increases the rotation speed of the screw so that the generator can generate electrical power, because the screw works at very low rotation speeds. Finally, the electrical generator, as the name suggests, transforms mechanical energy into electrical energy and this is fed into the electrical grid. These steps can be seen in Figure 3.5 [10].

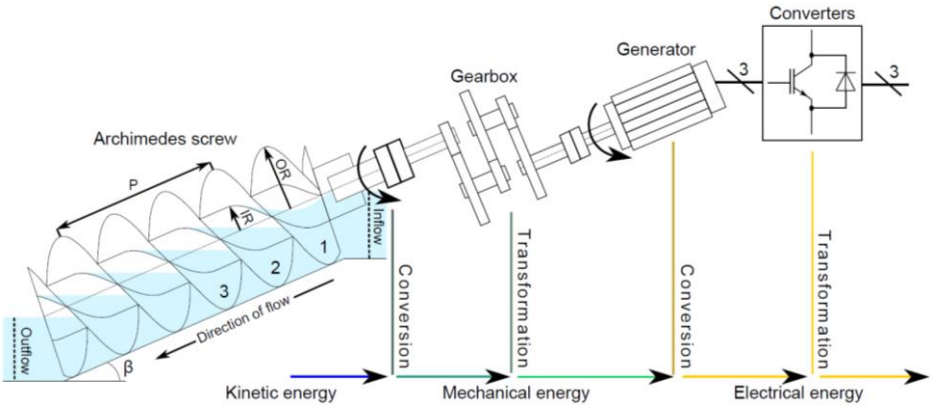

Figure 3.5 General principle of an Archimedes screw plant [10]

As mentioned above, the mechanical energy produced by the rotation of the screw is transformed in electricity using a generator. The power provided by the ASG is given by the following equation:

$$P_{ASG} = \rho\ g\ Q\ H\ \eta_{ASG} \qquad \text{Eq. 1}$$

With P_{ASG} the power in *Watt*, ρ the density of water in kgm^{-3}, g the gravitational constant (9.81 ms^{-2}), Q the flowrate in m^3s^{-1}, H the geodetic head in m and η_{ASG} the efficiency of the whole system.

There are several operating parameters in an ASG. The volume of water trapped between two successive blades is named "bucket" and we define it like V_B, the flow discharge Q, the rotational speed ω, the upstream water level h_{in} and the downstream water level h_{out}. Apart from these, the screw has its geometric parameters like the outer radius R_a, the inner radius R_i, the pitch of the screw S, the total length L, the threaded length L_B, the number of blades N and eventually the screw inclination β. All this parameters are shown in Figure 3.6.

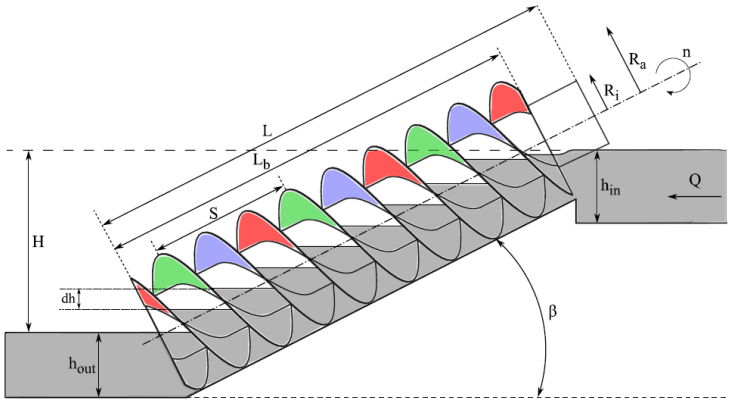

Figure 3.6 Geometrical parameters of the screw [3]

Although this study is going to focus on the screw as such, the efficiency of the system is directly proportional to the efficiency of the generator and transmission. This efficiency is related to leaks and losses caused by friction due to viscosity. To optimize the performance and efficiency of the whole system, it is necessary to minimize losses. The first flow loss (Q_f) occurs between the blades and the channel, and the second occurs when the screw is operating overfilled (Q_{over}). By neglecting the two flow leakages, the flowrate through the screw is equal to the product of the volume of water evacuated in one full rotation (360º) of the screw and the rotational speed. Then, the nominal flow is given by:

$$Q_{nom} = N\, V_B\, \frac{n}{60} \qquad \textit{Eq. 2}$$

Then, the total flowrate Q flowing in the screw is the sum of the nominal flow plus the both leakage mentioned above:

$$Q = Q_{nom} + Q_f + Q_{over} \qquad \textit{Eq. 3}$$

The hydraulic power available is, in *Watt*:

$$P_{hyd} = \rho\, g\, Q\, H \qquad \textit{Eq. 4}$$

The mechanical power provided by the screw is given by the product of the rotational speed and the torque:

$$P_{meca} = C_{screw}\,\omega \qquad \text{Eq. 5}$$

With P_{meca} the mechanical power in *Watt*, C_{screw} the axial torque delivered by the screw in *Nm* and ω the rotational speed of the screw in *rad* s^{-1}.

The turbine efficiency is then equal to:

$$\eta = \frac{P_{meca}}{P_{hyd}} \qquad \text{Eq. 6}$$

4. Computational Fluid Dynamics (CFD)

Computational fluid dynamics is a branch of fluid mechanics. It consists of analysing and solving problems involving fluid flows through numerical analysis and data structures. A CFD simulation uses various methods to solve the Navier-Stokes transport equations developed by Claude-Louis Navier in the early 1800s and improved by Sir George Stoke in the mid-1800s in Britain [7].

4.1. History of CFD

It was in the 1930s that the bidimensional methods were developed for solving the linearized potential equations. The first similar CFD calculations were in 1940 using ENIAC[1], although they were a failure. As early as the 1960s, a group of people at Los Alamos National Laboratory, USA, developed several numerical methods to simulate bidimensional transient fluid flows. This group of people was led by Francis H. Harlow (January 1928 – July 2016), considered one of the pioneers of CFD. Even so, it took some years for the field to be advanced enough to be useful for industry, as it also needed great computing power from computers.

As the years went by, some companies of the aerodynamic sector, like NASA or Boeing for example, developed several codes that allowed to approximate the problems and complement their final solution, along with the theory and experimental analysis. Nowadays the CFD is used as a very powerful and precise tool to predict and model the interaction with complex fluid flows [11].

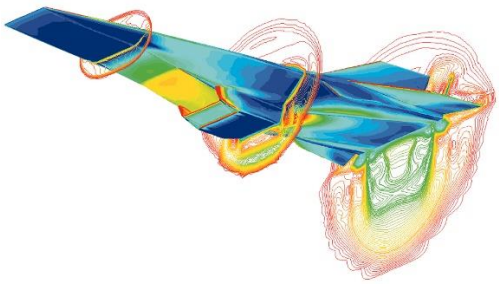

Figure 4.1 Computational Fluid Dynamics (CFD) Image of Hyper-X Research Vehicle at Mach 7 with Engine Operating [12]

[1] ENIAC (*Electronic Numerical Integrator and Computer*) was the first computer able to solve "a large class of numerical problems".

4.2. Governing equations

The fundamental basis of almost all CFD problems is the Navier-Stokes equations. These equations define many single-phase fluid flows, whether gas or liquid, and can be simplified by eliminating several terms to get the Euler equations. The Euler equations are obtained by simplifying the terms that describe viscous actions; if we simplify the terms that describe vorticity, we obtain the full potential equations. Finally, we can linearize the equations for small perturbations in subsonic and supersonic fluxes to get the linearized potential equations.

The system of equations consists of the continuity equation, momentum equation and the energy equation. The continuity equation of the Navier-Stokes equations is defined by:

$$\frac{\partial \rho}{\partial t} + \frac{\partial (\rho u)}{\partial x} + \frac{\partial (\rho v)}{\partial y} + \frac{\partial (\rho w)}{\partial z} = 0 \qquad \textit{Eq. 7}$$

with ρ the density, *t* the time, *u* the velocity in the x-direction, *v* de velocity in the y-direction, *w* the velocity in the z-direction, and the *x*, *y* and *z* the direction vectors. This equation (Eq. 7) is time dependent and is used to account for conservation of mass.

The conservation of momentum is accounted in the following system of three non-dimensional equations, which are time-dependent:

$$\frac{\partial (\rho u)}{\partial t} + \frac{\partial (\rho u^2)}{\partial x} + \frac{\partial (\rho uv)}{\partial y} + \frac{\partial (\rho uw)}{\partial z} = -\frac{\partial p}{\partial x} + \frac{1}{Re}\left[\frac{\partial \tau_{xx}}{\partial x} + \frac{\partial \tau_{xy}}{\partial y} + \frac{\partial \tau_{xz}}{\partial z}\right] \qquad \textit{Eq. 8}$$

$$\frac{\partial (\rho v)}{\partial t} + \frac{\partial (\rho uv)}{\partial x} + \frac{\partial (\rho v^2)}{\partial y} + \frac{\partial (\rho vw)}{\partial z} = -\frac{\partial p}{\partial y} + \frac{1}{Re}\left[\frac{\partial \tau_{xy}}{\partial x} + \frac{\partial \tau_{yy}}{\partial y} + \frac{\partial \tau_{yz}}{\partial z}\right] \qquad \textit{Eq. 9}$$

$$\frac{\partial (\rho w)}{\partial t} + \frac{\partial (\rho uw)}{\partial x} + \frac{\partial (\rho vw)}{\partial y} + \frac{\partial (\rho w^2)}{\partial z} = -\frac{\partial p}{\partial z} + \frac{1}{Re}\left[\frac{\partial \tau_{xz}}{\partial x} + \frac{\partial \tau_{yz}}{\partial y} + \frac{\partial \tau_{zz}}{\partial z}\right] \qquad \textit{Eq. 10}$$

with *p* the pressure, *Re* the Reynolds number, τ the stress and *q* the heat flux.

The last one, the energy equation (Eq. 11) is used to account for conservation of energy in the fluid system.

$$\frac{\partial(E_T)}{\partial t}+\frac{\partial(uE_T)}{\partial x}+\frac{\partial(vE_T)}{\partial y}+\frac{\partial(wE_T)}{\partial z} = -\frac{\partial(up)}{\partial x}-\frac{\partial(vp)}{\partial y}-\frac{\partial(wp)}{\partial z} + \frac{1}{Re}\left[\frac{\partial}{\partial x}\left(u\tau_{xx}+v\tau_{xy}+z\tau_{xz}\right)+\frac{\partial}{\partial y}\left(u\tau_{xy}+v\tau_{yy}+z\tau_{yz}\right) + \frac{\partial}{\partial z}\left(u\tau_{xz}+v\tau_{yz}+z\tau_{zz}\right)\right]-\frac{1}{Re\cdot Pr}\left[\frac{\partial q_x}{\partial x}+\frac{\partial q_y}{\partial y}+\frac{\partial q_z}{\partial z}\right] \quad \textit{Eq. 11}$$

with p the pressure, E_T the thermal energy component, Re the Reynolds number, τ the stress, q the heat flux and Pr de Prandtl Number.

With Navier-Stokes equations only approximations of solutions can be obtained using different flow resolution approaches. Only in some much idealized cases can it be reduced to an analytical solution. There are two types of flow solvers to solve the Navier-Stokes equations: the Eulerian solver and the Langrangian solver.

The Eulerian solvers are very efficient in solving flow near solid boundaries, although they require high computational power in order to solve the calculation, as high order refined mesh methods must be implemented to prevent them from dampening eddies and high intensity vortices near the boundaries [7]. For this method, the governing equations are solved with fixed coordinates inside a control volume [13]. This type of solver is the most common solution to this type of problems.

On the other hand, Langrangian solvers follow a parcel of fluid as it moves to approximate a solution. It has been demonstrated that this method, unlike Eulerian solvers, eliminates diffusion. The disadvantage of this technique is that modelling is less precise, more complex and requires much more computational power than Eulerian solvers [7].

4.3. Reynolds averaged Navier-Stokes equations (RANS)

Osborne Reynolds (1842 - 1912) developed an approximation of the Navier-Stokes equations averaged over time in order to solve the equations more easily. To do this, it was assumed that turbulent flows (in other words, time-dependent fluctuating flows) can be separated into two components: the time average and the fluctuating components. Using RANS is still computationally expensive but orders of magnitude lower than the standard Navier-Stokes equations. The following equation (Eq. 12) describes the x-direction vector before Reynolds's decomposition is applied to it:

$$\rho\left[\frac{\partial u}{\partial t}+u\frac{\partial u}{\partial x}+v\frac{\partial u}{\partial y}+w\frac{\partial u}{\partial z}\right]=-\frac{\partial p}{\partial x}+\mu\left[\frac{\partial u^2}{\partial x^2}+\frac{\partial^2 u}{\partial y^2}+\frac{\partial^2 u}{\partial z^2}\right] \quad \textit{Eq. 12}$$

Through a series of deductions and mathematical transformations, the RANS equation can be obtained which is shown as in equation 13 (Eq. 13) and is then used as the RANS equation in the solver:

$$\rho\left[\frac{\partial}{\partial x}(\bar{u}^2)+\frac{\partial}{\partial y}(\bar{u}\bar{v})+\frac{\partial}{\partial y}(\bar{u}\bar{w})\right] = -\frac{\partial \bar{p}}{\partial x} + \left[\frac{\partial}{\partial x}\left(\mu\frac{\partial \bar{u}}{\partial x}-\rho\overline{u'u'}\right)+\frac{\partial}{\partial y}\left(\mu\frac{\partial \bar{u}}{\partial y}-\rho\overline{u'v'}\right)+\frac{\partial}{\partial z}\left(\mu\frac{\partial \bar{u}}{\partial z}-\rho\overline{u'w'}\right)\right] \quad \text{Eq. 13}$$

The RANS system can be used to accurately approximate time-averaged solutions to the Navier-Stokes equations, while describing turbulent flows, because the RANS system divides velocity terms into both time-averaged and fluctuating components.

4.4. Turbulence models

A turbulence model is an equation (or system of equations) used to solve the stress tensor to close the RANS equations. There are several turbulence models that allow doing that: the simplest mode is the one that implements the "zero equation model". This model is very simple and quick to solve since it is used for a turbulence order that can normally be found experimentally. This model is not as accurate because it is assumed that all turbulence dissipates shortly after it is generated.

4.4.1. Spalart-Allmaras model

There is another single equation model called the Spalart-Allmaras model which is very popular and used for aerospace applications, although it is currently gaining prominence in turbomachinery applications. This model solves a single transport equation (Eq. 14) for the turbulent viscosity of the kinematic eddy [14]. This embodies a relatively new class of one-equation models in which it is not necessary to calculate a length scale related to the local shear layer thickness [15].

$$\frac{\partial}{\partial t}(\rho\bar{v})+\frac{\partial}{\partial x_i}(\rho\bar{v}u_i)=G_v+\frac{1}{\sigma_{\bar{v}}}\left[\frac{\partial}{\partial x_j}\left\{(\mu+\rho\bar{v})\frac{\partial \bar{v}}{\partial x_j}\right\}+C_{b2}\rho\left(\frac{\partial \bar{v}}{\partial x_j}\right)^2\right]-Y_v+S_{\bar{v}} \quad \text{Eq. 14}$$

with G_v the production of turbulent viscosity and Y_v the destruction of turbulent viscosity that occurs in the near-wall region due to wall blocking and viscous damping, σ_v and C_{b2} are constants and v the molecular kinematic viscosity and S_v a user-defined source term.

4.4.2. Two-equations models

Implementing a turbulence model with two equations that can explain more precisely and with a wider scale of turbulence is much more common and is the most used in CFD. The most implemented turbulence models are the k-ε model (k-epsilon) [16], the k-ω model (k-omega) [17], and the SST model (Menter's Shear Stress Transport model) [18].

For the k-epsilon model there are three main variants with small variations between them: standard [16], RNG [19] and Realizable [20]. The main changes between the three models are:

- The method for calculating turbulent viscosity.
- The turbulent Prandtl numbers governing the turbulent diffusion of k and ε.
- The generation and destruction terms in the ε equation.

4.4.2.1. Standard k-ε model

The k-ε model has become one of the main (and simplest) turbulence models of two transport equations. It is a very robust, economical and accurate model that can work with a wide range of turbulent flows and has therefore become a very popular model in the industry.

In the derivation of this model, it is assumed that the flow is completely turbulent and the effects of viscosity are negligible, therefore this model is only valid for totally turbulent flows.

The k-ε model uses two transport equations: one for the turbulence kinetic energy (*k*) (Eq. 15) and another to describe the dissipation velocity of the turbulence energy (ε) (Eq. 16).

$$\frac{\partial}{\partial t}(\rho k) + \frac{\partial}{\partial x_i}(\rho k u_i) = \frac{\partial}{\partial x_j}\left[\left(\mu + \frac{\mu_t}{\sigma_k}\right)\frac{\partial k}{\partial x_j}\right] + G_k + G_b - \rho\epsilon - Y_M + S_k \qquad \textit{Eq. 15}$$

$$\frac{\partial}{\partial t}(\rho \epsilon) + \frac{\partial}{\partial x_i}(\rho \epsilon u_i) = \frac{\partial}{\partial x_j}\left[\left(\mu + \frac{\mu_t}{\sigma_k}\right)\frac{\partial \epsilon}{\partial x_j}\right] + C_{1\epsilon}\frac{\epsilon}{k}(G_k + C_{3\epsilon}G_b) - C_{2\epsilon}\rho\frac{\epsilon^2}{k} + S_\epsilon \qquad \textit{Eq. 16}$$

where G_k is the generation of turbulence kinetic energy due to the mean velocity gradients, G_b is the generation of turbulence kinetic energy due to buoyancy, Y_M is the contribution of the fluctuating dilatation in compressible turbulence to the overall dissipation rate, $C_{1\epsilon}$, $C_{2\epsilon}$ and $C_{3\epsilon}$ are constants, σ_k and σ_ϵ are the turbulent Prandtl numbers for k and ϵ, respectively, and S_k and S_ϵ are user-defined source terms.

The turbulent viscosity μ_t is computed by combining k and ε as follows, where C_μ is a constant:

$$\mu_t = \rho C_\mu \frac{k^2}{\epsilon} \qquad \text{Eq. 17}$$

In this model, constants ($C_{1\epsilon}$, $C_{2\epsilon}$, C_μ, σ_k and σ_ϵ) have a default value determined with several experiments with air and water for fundamental turbulent shear flows including homogeneous shear flows and decaying isotropic grid turbulence. They have been found to work fairly well for a wide range of a wall-bounded and free shear flows. The model constants have the following default values:

$$C_{1\epsilon} = 1.44, C_{2\epsilon} = 1.92, C_\mu = 0.09, \sigma_k = 1.0, \sigma_\epsilon = 1.3$$

4.4.2.2. RNG k-ε model

The RNG model is similar in shape to the standard k-ε model, but includes refinements to the standard model that make it a more accurate and reliable model for a wider range of flows [19]. These refinements are as follows:

- The effect of the swirl on the turbulence is included, which enhances the accuracy of the swirl flows.
- It has an additional term in its epsilon equation that significantly improves the accuracy of rapidly strained flows.
- It provides an analytical formula for turbulent Prandtl numbers, while the standard epsilon model uses constant values specified by the user.
- While the standard k-ε model is a high-Reynolds-number model, the RNG theory provides an analytically-derived differential formula for effective viscosity that accounts for low-Reynolds-number effects. Effective use of this feature does, however, depend on an appropriate treatment of the near-wall region.

The transport equations for the RNG k-ε model are very similar as the standard model, but with small differences:

$$\frac{\partial}{\partial t}(\rho k) + \frac{\partial}{\partial x_i}(\rho k u_i) = \frac{\partial}{\partial x_j}\left(\sigma_k \mu_{eff} \frac{\partial k}{\partial x_j}\right) + G_k + G_b - \rho\epsilon - Y_M + S_k \qquad \text{Eq. 18}$$

$$\frac{\partial}{\partial t}(\rho \epsilon) + \frac{\partial}{\partial x_i}(\rho \epsilon u_i) = \frac{\partial}{\partial x_j}\left(\sigma_k \mu_{eff} \frac{\partial \epsilon}{\partial x_j}\right) + C_{1\epsilon}\frac{\epsilon}{k}(G_k + C_{3\epsilon}G_b) - C_{2\epsilon}\rho\frac{\epsilon^2}{k} - R_\epsilon + S_\epsilon \qquad \text{Eq. 19}$$

with G_k the generation of turbulence kinetic energy due to the mean velocity gradients, G_b the generation of turbulence kinetic energy due to buoyancy, Y_M the contribution of the fluctuating dilatation in compressible turbulence to the overall dissipation rate. The quantities σ_k and σ_ϵ are the inverse effective Prandtl number for k and ϵ, respectively, and S_k and S_ϵ are user-defined source terms.

This model better handles low Reynolds and near-wall flows, as the differential equation for turbulent viscosity (Eq. 20) is integrated to obtain an accurate description of how effective turbulent transport varies with Reynolds effective number (or eddy scale).

$$d\left(\frac{\rho^2 k}{\sqrt{\epsilon\mu}}\right) = 1.72\frac{\hat{v}}{\sqrt{\hat{v}^3 - 1 + C_v}}d\hat{v} \qquad \textit{Eq. 20}$$

where

$$\hat{v} = \mu_{eff}/\mu\,, C_v \approx 100$$

In the high-Reynolds-number limit, the differential equation for turbulent viscosity gives:

$$\mu_t = \rho\, C_\mu \frac{k^2}{\epsilon} \qquad \textit{Eq. 21}$$

with $C_\mu = 0.0845$, derived using RNG theory. It is interesting to note that this value of C_μ is very close to the empirically-determined value of 0.09 used in the standard k-ε model.

The main difference between the RNG and the standard k-ε models lies in the additional term R_ϵ in the ϵ equation given by:

$$R_\epsilon = \frac{C_\mu \rho \eta^3 (1 - \eta/\eta_0)}{1 + \beta\eta^3}\frac{\epsilon^2}{k} \qquad \textit{Eq. 22}$$

where $\eta \equiv Sk/\epsilon\,, \eta_0 = 4.38, \beta = 0.012.$

Rearranging the equation 19 (Eq. 19) using the equation 22 (Eq. 22), and the resulting ϵ equation (Eq. 23) can be rewritten as:

$$\frac{\partial}{\partial t}(\rho\epsilon) + \frac{\partial}{\partial x_i}(\rho\epsilon u_i) = \frac{\partial}{\partial x_j}\left(\sigma_k \mu_{eff}\frac{\partial\epsilon}{\partial x_j}\right) + C_{1\epsilon}\frac{\epsilon}{k}(G_k + C_{3\epsilon}G_b) - C^*_{2\epsilon}\rho\frac{\epsilon^2}{k} \qquad \textit{Eq. 23}$$

where $C^*_{2\epsilon}$ is given by

$$C^*_{2\epsilon} \equiv C_{2\epsilon} + \frac{C_\mu \rho \eta^3 (1 - \eta/\eta_0)}{1 + \beta\eta^3} \qquad \textit{Eq. 24}$$

In regions where $\eta < \eta_0$, the *R* term makes a positive contribution, and $C^*_{2\epsilon}$ becomes larger than $C_{2\epsilon}$. In the logarithmic layer, for instance, it can be shown that $\eta \approx 3.0$, giving $C^*_{2\epsilon} \equiv 2.0$, which is close in magnitude to the value of $C_{2\epsilon}$ in the standard k-ε model. As a result, for weakly to moderately strained flows, the RNG model tends to give results largely comparable to the standard k-ε model.

Otherwise, in regions where $\eta > \eta_0$ (large strain rate), the R term makes a negative contribution, making the value of $C_{2\epsilon}^*$ less than $C_{2\epsilon}$. In comparison with the standard k-ε model, the smaller destruction of ϵ augments ϵ, reducing k and the effective viscosity. As a result, in rapidly strained flows, the RNG model yields a lower turbulent viscosity than the standard k-ε model.

In certain flow classes, the performance of the RNG model is superior to the standard model, as it responds better to the effects of rapid strain and aerodynamic curvature.

The inverse effective Prandtl numbers, σ_k and σ_ϵ, are computed using the following formula derived analytically by the RNG theory:

$$\left|\frac{\alpha - 1.3929}{\alpha_0 - 1.3929}\right|^{0.6321} \left|\frac{\alpha + 2.3929}{\alpha_0 + 2.3929}\right|^{0.3679} = \frac{\mu_{mol}}{\mu_{eff}} \qquad \text{Eq. 25}$$

where $\alpha_0 = 1.0$. In the high-Reynolds-number limit ($\mu_{mol}/\mu_{eff} \ll 1$), $\alpha_k = \alpha_\epsilon \approx 1.393$.

4.4.2.3. Realizable k-ε model

The realizable k-ε model is a relatively new and developing model. Realizable means that the model satisfies certain mathematical constraints on Reynolds tensions that the other two k-ε models did not. This model differs from the standard model in two ways:

- The realizable k-ε model contains a new formulation for the turbulent viscosity.
- A new transport equation for the dissipation rate (ϵ) has been derived from an exact equation for the transport of the mean-square vorticity fluctuation.

An immediate advantage of the realizable k-epsilon model is that it more accurately predicts the dispersion dose of both planar and round jets. It is also likely to provide superior performance to other models for flows involving rotation, boundary layers under strong adverse pressure gradients, separation and recirculation.

As the model is relatively new, it is not very clear in which cases it systematically outperforms the RNG model, however, studies have shown that the workable model provides the best performance of all versions of the k-epsilon model for several validations of separated flows and flows with complex secondary flow features. However, both the realizable model and the RNG have shown substantial improvements over the standard model, where flow characteristics include strong aerodynamic curvature, vortices or rotation.

A limitation of this model is that it produces non-physical turbulent viscosities in situations where the computational domain contains both rotary and stationary fluid zones, e.g. multiple

reference frames or rotary sliding meshes. This is because it includes the effects of medium rotation on the definition of turbulent viscosity.

The modeled transport equations for the turbulence kinetic energy (*k*) (Eq. 26) and the dissipation velocity of the turbulence energy (ε) (Eq. 27) are:

$$\frac{\partial}{\partial t}(\rho k) + \frac{\partial}{\partial x_i}(\rho k u_j) = \frac{\partial}{\partial x_j}\left[\left(\mu + \frac{\mu_t}{\sigma_k}\right)\frac{\partial k}{\partial x_j}\right] + G_k + G_b - \rho\epsilon - Y_M + S_k \qquad \textit{Eq. 26}$$

$$\frac{\partial}{\partial t}(\rho\epsilon) + \frac{\partial}{\partial x_i}(\rho\epsilon u_j) = \frac{\partial}{\partial x_j}\left[\left(\mu + \frac{\mu_t}{\sigma_\epsilon}\right)\frac{\partial \epsilon}{\partial x_j}\right] + \rho C_1 S_\epsilon - \rho C_2 \frac{\epsilon^2}{k + \sqrt{v\epsilon}} + C_{1\epsilon}\frac{\epsilon}{k} C_{3\epsilon} B_b + S_\epsilon \qquad \textit{Eq. 27}$$

where

$$C_1 = max\left[0.43, \frac{\eta}{\eta + 5}\right], \eta = S\frac{k}{\epsilon}, S = \sqrt{2S_{ij}S_{ij}}$$

with G_k the generation of turbulence kinetic energy due to the mean velocity gradients, G_b the generation of turbulence kinetic energy due to buoyancy, Y_M the contribution of the fluctuating dilatation in compressible turbulence to the overall dissipation rate, C_2 and $C_{1\epsilon}$ are constants, σ_k and σ_ϵ are the inverse effective Prandtl number for k and ϵ, respectively, and S_k and S_ϵ are user-defined source terms.

The model constants have been established to ensure that the model performs well for certain canonical flows. The model constants are:

$$C_{1\epsilon} = 1.44, C_2 = 1.9, \sigma_k = 1.0, \sigma_\epsilon = 1.2$$

The eddy viscosity is defined by:

$$\mu_t = \rho C_\mu \frac{k^2}{\epsilon} \qquad \textit{Eq. 28}$$

The difference between the realizable k-ε model and the standard and RNG k-ε models is that C_μ is no longer constant. For an inertial sublayer in an equilibrium boundary layer the equation 29 (Eq. 29) recover the standard value of 0.09. It is defined by:

$$C_\mu = \frac{1}{A_0 + A_s \frac{kU^*}{\epsilon}} \qquad \textit{Eq. 29}$$

where

$$U^* = \sqrt{S_{ij}S_{ij} + \widetilde{\Omega}_{ij}\widetilde{\Omega}_{ij}} \quad \text{Eq. 30}$$

with

$$\widetilde{\Omega}_{ij} = \Omega_{ij} - 2\epsilon_{ijk}\omega_k;\ \Omega_{ij} = \overline{\Omega_{\iota J}} - \epsilon_{ijk}\omega_k$$

where $\overline{\Omega_{\iota J}}$ is the mean rate-of-rotation tensor viewed in a rotating reference frame with the angular velocity ω_k. The constants A_0 and A_S are given by

$$A_0 = 4.04, A_S = \sqrt{6}\cos\phi$$

where

$$\phi = \frac{1}{3}\cos^{-1}\left(\sqrt{6}W\right),\ \ W = \frac{S_{ij}S_{jk}S_{ki}}{\tilde{S}^3},\ \ \tilde{S} = \sqrt{S_{ij}S_{ij}}, S_{ij} = \frac{1}{2}\left(\frac{\partial u_j}{\partial x_i} + \frac{\partial u_i}{\partial x_j}\right)$$

As mentioned above, this model includes the effects of medium rotation on the definition of turbulent viscosity. This extra rotation effect has demonstrated superior behaviour to the standard model, however, its application to multiple reference systems should be taken with some caution.

4.4.2.4. Standard k-ω model

This model works similarly to the k-ε model in that it uses two equations to describe the transported turbulence variables. It is an empirical model based on the transport equations of the model for the turbulence kinetic energy (k) (Eq. 31) and the specific dissipation rate (ω) (Eq. 32) [7].This model is applicable to wall flows and free shear flows, as it predicts free shear spreading flows that are in close agreement with the measurements of distant wakes, mixing layers and plane, round and radial jets [21]. The k-ω model works best in the inner region of the boundary layer.

$$\frac{\partial(\rho k)}{\partial t} + \frac{\partial(\rho k u_i)}{\partial x_i} = \frac{\partial}{\partial x_j}\left[\left(\mu + \frac{\mu_t}{\sigma_k}\right)\frac{\partial k}{\partial x_j}\right] + G_k - Y_k + S_k \quad \text{Eq. 31}$$

$$\frac{\partial(\rho \omega)}{\partial t} + \frac{\partial(\rho w u_i)}{\partial x_i} = \frac{\partial}{\partial x_j}\left[\left(\mu + \frac{\mu_t}{\sigma_\omega}\right)\frac{\partial \omega}{\partial x_j}\right] + G_\omega - Y_\omega + S_\omega \quad \text{Eq. 32}$$

where G_k represents the generation of turbulence kinetic energy due to mean velocity gradients, G_ω represents the generation of ω, Y_k and Y_ω represent the dissipation of k and ω due to turbulence, σ_k

and σ_ω are the inverse effective Prandtl number for *k* and ω, respectively, and S_k and S_ω are user-defined source terms.

The turbulent viscosity (Eq. 33) is described as a function of the turbulence kinetic energy (k) and specific rate of dissipation of the turbulence kinetic energy (ω):

$$\mu_t = \alpha^* \frac{\rho k}{\omega} \qquad \textit{Eq. 33}$$

where the coefficient α^* damps the turbulent viscosity causing a low-Reynolds-number correction.

The model constants are:

$$\sigma_k = 2.0, \sigma_\omega = 2.0$$

4.4.2.5. Shear-Stress Transport (SST) k-ω model

The Menter's shear stress transport model (SST model) was developed to mix the optimum use of the k-ε and k-ω models, implements them where they are most accurate. It is the two equation model most used in CFD as it was designed to overcome the two limitations of the k-epsilon and k-omega model. The SST model blend the robust and accurate formulation of the k-ω model in the near-wall region with the free-stream independence of the k-ε model in the far field.

This method can be used to predict, with a high degree of accuracy, the onset of flow separation, as well as the amount of flow separation in a simulation, as it includes the effects of transport on the formulation of eddy viscosity [7].

The SST k-ω model is similar to the standard k-ω model, but includes the following refinements [22]:

- The standard k-ω model and the transformed k-ε model are both multiplied by a blending function and both models are added together. The blending function is designed to be one in the near-wall region, which activates the standard k-ω model, and zero away from the surface, which activates the transformed k-ε model.
- The SST model incorporates a damped cross-diffusion derivate term in the ω equation.
- The definition of the turbulent viscosity is modified to account for the transport of the turbulent shear stress.
- The modelling constants are different.

The transport equations for the SST k-ω model are given by:

$$\frac{\partial(\rho k)}{\partial t}+\frac{\partial(\rho k u_i)}{\partial x_i}=\frac{\partial}{\partial x_j}\left[\left(\mu+\frac{\mu_t}{\sigma_k}\right)\frac{\partial k}{\partial x_j}\right]+\tilde{G}_k-Y_k+S_k \quad \text{Eq. 34}$$

$$\frac{\partial(\rho k)}{\partial t}+\frac{\partial(\rho w u_i)}{\partial x_i}=\frac{\partial}{\partial x_j}\left[\left(\mu+\frac{\mu_t}{\sigma_\omega}\right)\frac{\partial \omega}{\partial x_j}\right]+\frac{\alpha}{v_t}G_k-Y_\omega+D_\omega+S_\omega \quad \text{Eq. 35}$$

where $\tilde{G}_k$ represents the production of turbulence kinetic energy, Y_k and Y_ω represent the dissipation of k and ω due to turbulence, D_ω is the term of cross-diffusion introduced to blend the two models together, σ_k and σ_ω are the inverse effective Prandtl number for k and ω, respectively, and S_k and S_ω are user-defined source terms. All of this terms are given by:

$$\sigma_k=\frac{1}{F_1/\sigma_{k,1}+(1-F_1)/\sigma_{k,2}} \quad \text{Eq. 36}$$

$$\sigma_w=\frac{1}{F_1/\sigma_{\omega,1}+(1-F_1)/\sigma_{\omega,2}} \quad \text{Eq. 37}$$

$$\tilde{G}_k=\min(G_k,10\rho\beta^*k\omega) \quad \text{Eq. 38}$$

$$Y_k=\rho\beta^*k\omega \quad \text{Eq. 39}$$

$$Y_\omega=\rho\beta\omega^2 \quad \text{Eq. 40}$$

$$D_\omega=2(1-F_1)\rho\sigma_{\omega,2}\frac{1}{\omega}\frac{\partial k}{\partial x_j}\frac{\partial \omega}{\partial x_j} \quad \text{Eq. 41}$$

The turbulent viscosity is defined by:

$$\mu_t=\frac{\rho k}{\omega}\frac{1}{max\left[\frac{1}{a^*},\frac{SF_2}{a_1\omega}\right]} \quad \text{Eq. 42}$$

The blending functions F_1 and F_2 are given by:

$$F_1=\tanh(\phi_1^4) \quad \text{Eq. 43}$$

$$F_2=\tanh(\phi_2^2) \quad \text{Eq. 44}$$

$$\phi_1=min\left[\max\left(\frac{\sqrt{k}}{0.09\omega y},\frac{500\mu}{\rho y^2\omega}\right),\frac{4\rho k}{\sigma_{\omega,2}D_\omega^+y^2}\right] \quad \text{Eq. 45}$$

$$D_{\omega}^{+} = max\left[2\rho\frac{1}{\sigma_{\omega,2}}\frac{1}{\omega}\frac{\partial k}{\partial x_j}\frac{\partial \omega}{\partial x_j}, 10^{-10}\right] \quad \textit{Eq. 46}$$

$$\phi_2 = max\left[2\frac{\sqrt{k}}{0.09\omega y}, \frac{500\mu}{\rho y^2 \omega}\right] \quad \textit{Eq. 47}$$

The model constants are:

$$\sigma_{k,1} = 1.176, \sigma_{\omega,1} = 2.0, \sigma_{k,2} = 1.0, \sigma_{\omega,2} = 1.168, a_1 = 0.31$$

4.5. Free surface modelling

It is necessary to accurately determine the evolution of free surface flow occurring within an Archimedes screw generator. A surface between a gas and a liquid is often referred to as a free surface. The free word arises from the great difference in densities between gas and liquid, which allow the liquid to move freely with respect to the gas. The only influence that the gas has on the liquid is the pressure it exerts on the liquid surface.

Free surfaces require the introduction of special methods to define their location, their movement and their influence on a flow.

4.5.1. Lagrangian Grid Methods

Many finite element methods use the simplest way to define and follow a free surface, which is to build a Lagrangian grid that moves with the fluid. Because grid and fluid move together, the grid automatically tracks free surfaces. On a surface it is necessary to modify the approximation equations to include the proper contour conditions and to take into account the fact that the fluid exists only on one side of the contour.

The main limitation of Lagrangian methods is that they cannot track surfaces that break or intersect. Large amplitude surface movements can be difficult to track without the introduction of regridding techniques such as the Arbitrary-Lagrangian-Eulerian (ALE) method.

The idea of the Arbitrary Lagrangian-Eulerian (ALE) method is to assign a specific velocity to the mesh in order to follow the movements of the domain. The originality of the method is that this velocity is not the actual velocity of particles of water [23].

4.5.2. Marker-and-Cell (MAC) Method

The MAC method is a method developed at the Los Alamos National Laboratory to simulate incompressible fluid flow properly without excessive distortion [7]. This numerical method was the first method for time-dependent flow and free surface problems. It is based on a fixed Eulerian network of control volumes. The location of the fluid within the grid is determined by a set of marker particles that move with the fluid, but have no physical properties such as volume or mass [24].

Cells containing markers are considered occupied by the fluid, while those without markers are empty. A free surface is defined to exist in any grid cell that contains particles and also has at least one neighbouring grid cell that is empty. Some special treatments are required to define fluid properties in newly filled grid cells and to cancel them from empty cells. Gas pressure was assigned to all surface cells, as well as velocity components inside or outside the surface so that contour, incompressibility and zero shear stress conditions on the surface could be approximated.

One of the main reasons why this method is so successful is that the markers do not track the surfaces directly, instead they track the fluid volumes. Surfaces are simply the limits of volumes, and in this sense surfaces can appear, merge, or disappear as volumes separate or merge [24].

The main inconvenience is the time cost for additional calculation to follow the particles, in addition to the resolution of equations governing the movement of the fluid [23]. Another limitation of marker particles is that, in converging or diverging flows, they do not do a good job of tracking flow processes, since markers follow the centroids of small fluid elements, but when these are drawn into long convoluted strands, markers can cease to be good indicators of fluid configuration [24].

4.5.3. Volume-of-Fluid (VOF) method

This model originated to have the powerful fluid volume tracking feature of the MAC method but without its large memory and CPU costs. The VOF model is based on the concept of a fluid volume fraction. Knowing the amount of fluid in each cell makes it possible to locate surfaces, since surfaces will not fill the cell at all, as well as determine surface slopes and curvatures, which are calculated using fluid volume fractions in neighbouring cells [24].

The governing equation of the VOF method is expressed as:

$$\frac{DF}{Dt} = \frac{\partial F(\vec{x}t)}{\partial t} + \left(\vec{V}.\nabla\right) F(\vec{x}t) = 0 \qquad \textit{Eq. 48}$$

where F is a function having a value of unity at any point in the fluid.

For a cell full of fluid a unit value of F is used, for a cell that contains no fluid a zero value of F is used and a cell that has a value between one and zero contains a free surface. If the volume fraction of q^{th} fluid in the cell is denoted as α_q, then three conditions are possible as given below [25]:

- $\alpha_q = 0 \rightarrow$ the cell is empty of the q^{th} fluid
- $\alpha_q = 1 \rightarrow$ the cell is full of the q^{th} fluid
- $0 < \alpha_q < 1 \rightarrow$ the cell contains the interface between the q^{th} fluid and one or more other fluids

The VOF formulation applies the concept that two or more fluids (or phases) are not interpenetrating. For each additional phase a variable is introduced with the volume fraction of the phase in the computational cell. The fields for all variables and properties are shared by the phases and represent volume-averaged values, as long as the volume fraction of each of the phases is known at each location. Thus the variables and properties in any particular cell are either purely representative of one of the phases, of representative of a mixture of the phases, depending upon the values of volume fraction [25].

5. Computational modelling

Understanding the motion of liquids and gases is crucial in many branches of engineering. Until recently, studies of fluids in motion were confined to the laboratory, but with the rapid growth in processing power of the personal computer, software applications now bring numerical analysis and solutions of flow problem to the desktop [26].

Computational Fluid Dynamics (CFD) has become a fundamental part of design and analysis in the engineering industry in order to predict the behaviour of new designs before they are ever manufactured. CFD solutions from ANSYS, Inc. are based on the proven technology of ANSYS® CFX® software [26].

CFX technology is available in the ANSYS® Workbench™ interface. Geometry creation, meshing, physics definition, solution and post-processing for CFD are available in a single simulation environment, allowing easy performance of simulation from geometry to post-processing.

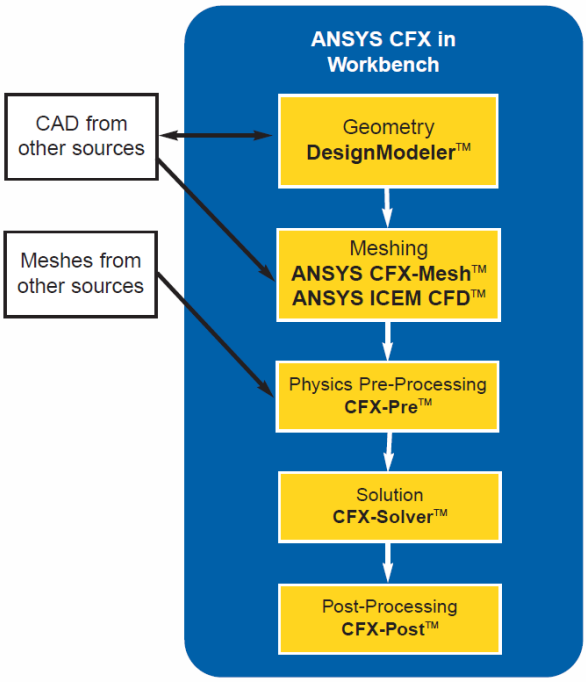

Figure 5.1 Ansys CFX in Workbench structure [26]

For this thesis the Workbench interface with the Ansys Fluent solver has been used. For the geometry the Spacelaim software integrated into Workbench was used, then the geometry was meshed with Ansys Meshing and finally the Ansys Fluent software was used to perform the simulations.

5.1. Geometry

As mentioned above, this thesis performs simulations of an Archimedean screw. The CAD geometry was provided by an engineering consultancy in Regensburg, Germany. The geometry of the entire hydroelectric plant was received as shown in the Figure 5.2.

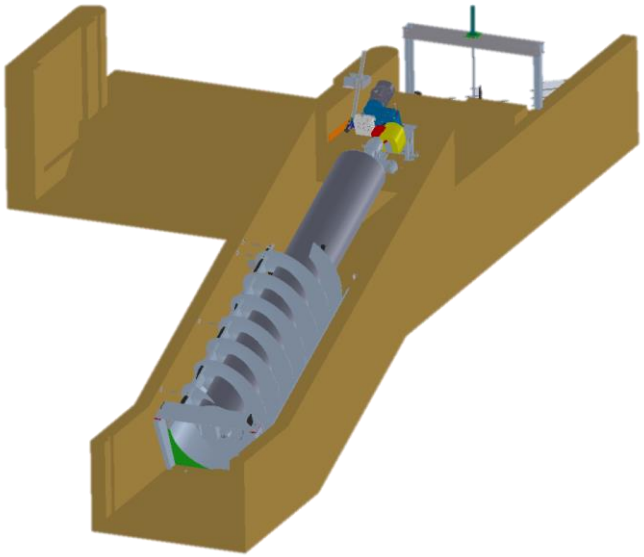

Figure 5.2 Archimedes Screw Generator

The screw as such has three blades and a total length of 7425mm. It will be placed in the hydroelectric plant in such a way that it will have an inclination of 22° as shown in the Figure 5.2. The geometrical parameters of the screw are defined in Table 1.

Geometric parameter	Nomenclature	Value	Unit
Inner radius	R_i	508	mm
Outer radius	R_a	950	mm
Threaded length	L_B	4400	mm
Total length	L	7425	mm
Pitch of the screw	S	1907	mm
Number of blades	N	3	-
Inclination	β	22	°

Table 1 Geometric parameters of the screw

In order to perform a CFD simulation, it was necessary to extract the negative from the existing screw CAD geometry (Figure 5.3). This step was done with the SpaceClaim software inside the Workbench interface.

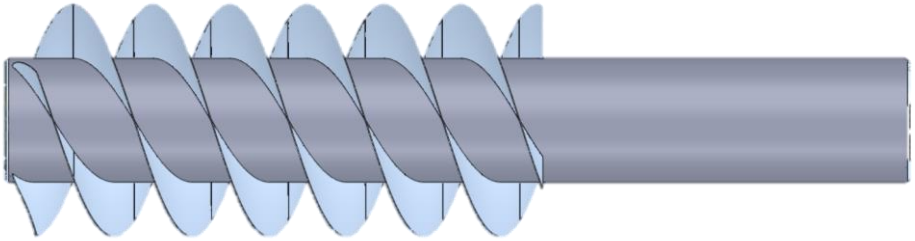

Figure 5.3 Archimedes screw

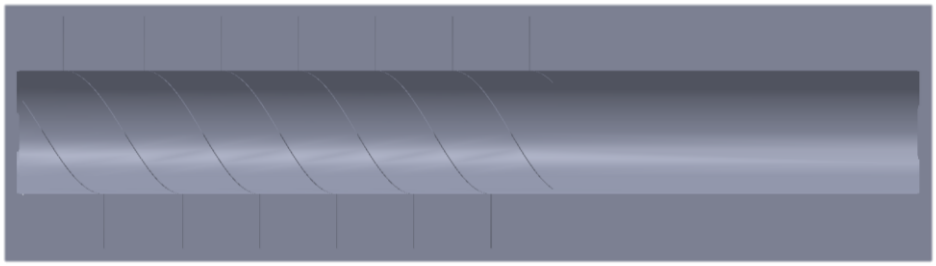

Figure 5.4 Negative

Two small nozzles were added to the negative to give it the 22º inclination that the generator has in the real plant. The final geometry would be as shown in the Figure 5.5:

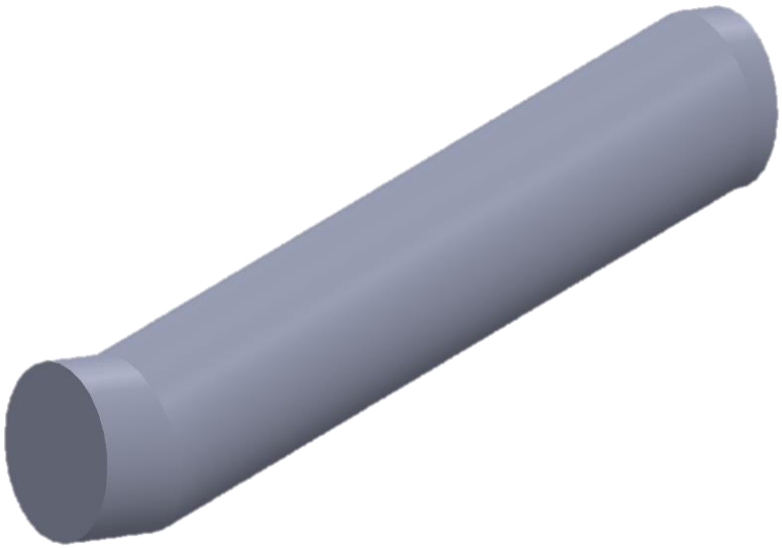

Figure 5.5 FInal geometry

5.2. Mesh

For meshing, a mesh with a tetrahedral element size of 0.0675m has been used, and the final result is a mesh formed by 507788 elements and 101044 nodes, as shown in the images below (Figure 5.6 and Figure 5.7).

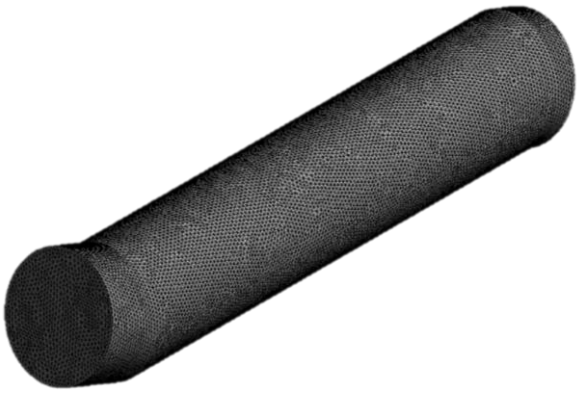

Figure 5.6 Final geometry meshed

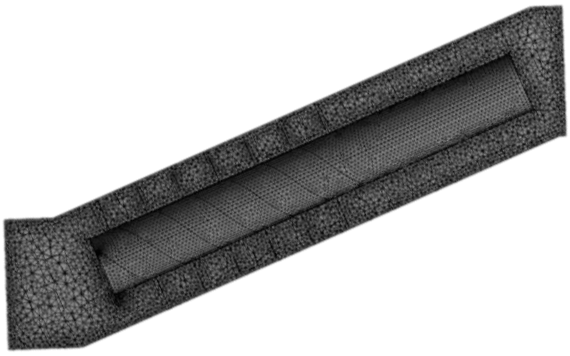

Figure 5.7 Section plane of the mesh

The mesh was constructed in this way with the intention of optimizing the relationship between the calculation time and the validity of the results. If a highly refined mesh was constructed, in other words, with a lot of elements, the calculation time would increase considerably. Meshes of up to 3 million elements were tested, but when the simulation was calculated, it took a very long time to calculate. That's why, after several tests with different meshes, it was decided to establish a mesh of half a million elements and consider it as good.

In addition, a dynamic mesh was created in order to simulate the rotation of the screw. The dynamic mesh was created by introducing a rotation speed set with a UDF file previously compiled in the program. It was done in this way, since with this file, a significant amount of computational memory is saved to the program and allows to concentrate the memory on the calculation of the mesh, and not on simulating the movement, thus reducing the calculation time. The dynamic mesh was configured

as long as it worked with the smoothing and remeshing methods. These methods are included in the Dynamic Mesh section of Ansys Fluent. Their settings had to be configured in order for the mesh to function correctly, as shown in the appendices [Appendix].

5.3. Turbulence and free surface flow modelling

In these simulations, an incompressible, turbulent and multiphase fluid has been modeled. In addition, to take into account the rotation of the screw, a dynamic mesh has been used, as explained in the previous section.

The continuity equation for an incompressible flow is:

$$\nabla \cdot \mathrm{U} = 0 \qquad \textit{Eq. 49}$$

The momentum equation with Boussinesq eddy viscosity assumption can be written in compact form:

$$\frac{\partial U}{\partial t} + \nabla \cdot (UU) = -\nabla \mathrm{P} + \nabla\big((v + v_t)\nabla \mathrm{U}\big) \qquad \textit{Eq. 50}$$

with *U* the velocity, v the kinematic viscosity of the fluid and v_t the turbulent viscosity.

The SST k-ω model has been chosen to solve the Reynolds averaged Navier-Stokes (RANS) equations because that takes advantage of k-ε formulation in the free-stream and k-ω ones in near-wall domain with low *Re* values, and also, because of its wide applicability range. As mentioned in section 4.4.2.5, the value of the turbulent viscosity is given by the following equation:

$$v_t = \frac{k}{\omega} \frac{1}{max\left[\frac{1}{a^*}, \frac{SF_2}{a_1 \omega}\right]} \qquad \textit{Eq. 51}$$

with *k* the turbulence intensity, ω the turbulence dissipation rate, *S* the strain rate magnitude, F_2 a blending function, a^*a damping coefficient of turbulent viscosity and $a_1$the model constant taken equal to 0.31, as said in the section 4.4.2.5.

The free surface position is determined thanks to the Volume Of Fluid (VOF) method. It is a powerful method for incompressible flows with two non-miscible phases like water and air [27], as in this case. It uses cell's filling to determine the time evolution of flow in a meshed area. This method was chosen because it is widely used and validated in different multiphase flows problems [3].

5.4. Boundary conditions

The boundary conditions used in the simulations are those shown in the following table:

Flow condition	Nomenclature	Value	Unit
Rotational speed of the screw	n	10 - 20	rpm
Velocity inlet of water	v	0,5 - 3	$m\ s^{-1}$
Flow rate	Q	0,87 - 5,20	$m^3\ s^{-1}$

Table 2 Flow conditions

The rotation speeds were chosen arbitrarily with this value, only with the knowledge that this type of generator works at low rotation speeds. The same happens with the inlet flows and all the boundary conditions, some previous publications ([27], [3]) were consulted and an attempt was made to scale more or less to the model shown in those articles.

There are also three values that are constant, but that appear in the equations and are therefore necessary for the calculation of the efficiency of the screw, which are the following:

Boundary condition	Nomenclature	Value	Unit
Gravity	g	9,81	$m\ s^{-2}$
Density of the water	ρ	1000	$kg\ m^{-3}$
Hydraulic head	H	1,05	m

Table 3 Boundary conditions constant

5.5. Turbine modelling

As mentioned in section 3.2.2, the turbine efficiency is determined with the following equations:

$$P_{hyd} = \rho\ g\ Q\ H \qquad \textit{Eq. 52}$$

$$P_{meca} = C_{screw}\ \omega \qquad \textit{Eq. 53}$$

$$\eta = \frac{P_{meca}}{P_{hyd}} \qquad \textit{Eq. 54}$$

where

$$\omega = n2\pi/60$$

These equations require the values of the torque provided by the screw C_{screw}, the hydraulic head H, the rotational speed n in rpm and the flow rate Q, as the density of the water and the gravity. These last two, are constants, as well as the hydraulic head that is determined from inlet and outlet water heights, in other words, it is constant in all simulations (as shown in the Table 3). Both the rotation speed and the flow rate are fixed in each simulation, so only the value of the torque needs to be obtained.

The elementary force induced by the fluid pressure is equal to:

$$d\vec{F}_p = dA \cdot P_f \cdot \vec{n} \qquad \text{Eq. 55}$$

with dA the elementary surface in m^2, P_f the pressure of the fluid exerted on dA in Nm^{-2}, and $\vec{n}$ the surface normal vector.

The shear stress due to viscosity of the fluid is defined by:

$$\tau = \rho \cdot (v_t + v)\frac{\partial U}{\partial n} \qquad \text{Eq. 56}$$

with ρ the density in kgm^{-3}, v the kinematic viscosity in m^2s, v_t the kinematic turbulent viscosity in m^2s, τ the shear stress and U the fluid velocity in ms^{-1}. Wall functions are used to determine v_t and the velocity in the boundary layer.

The total torque provided by the screw projected on its axis is:

$$C_{screw} = C_p - C_v \qquad \text{Eq. 57}$$

where C_p is the torque induced by the pressure exerted by the fluid on the screw and C_v is the torque due to the fluid viscosity. As it can be seen in the equation (Eq. 57), the first one is a generator torque whereas the second one is a brake torque.

6. Results and discussion

In this thesis, a total of 8 simulations have been performed with the different boundary conditions mentioned in section 5.4. Two different rotational speeds were imposed, and with each rotational speed simulations were made with four different inlet flow rates, as shown in the table of results (Table 4).

With the results of the torque obtained through Ansys Fluent Post, the hydraulic power (Eq. 52) and mechanical power (Eq. 53) were calculated, and with these two, the efficiency was calculated with the equation mentioned in section 5.5 (Eq. 54).

Rotational speed (rpm)	**Velocity inlet ($m\ s^{-1}$)**	**Flow rate ($m^3\ s^{-1}$)**	**Torque (N m)**	**Mechanical power (W)**	**Hydraulic power (W)**	**Efficiency**
n	**v**	**Q**	**C**	**P_{mec}**	**P_{hyd}**	**η**
10	0,5	0,87	6127	6416,174	8919,21	0,71936568
	1	1,73	11040	11561,051	17838,42	0,64809834
	2	3,46	26507	27758,042	35676,84	0,77804088
	3	5,20	27038	28314,103	53515,26	0,52908463
20	0,5	0,87	5181	10851,052	8919,21	1,2165933
	1	1,73	7451	15605,325	17838,42	0,87481535
	2	3,46	13781	28862,835	35676,84	0,80900754
	3	5,20	22593	47318,629	53515,26	0,88420808

Table 4 Table of results

The first behaviour that we can observe in the results is the increase of the torque as the velocity of the inlet flow increases. This is demonstrated in the equation mentioned above (Eq. 55), and gives physical meaning to the results obtained in the simulations.

As can be seen in the table of results (Table 4), the values obtained from the torque with the rotation speed of 10rpm are higher than those obtained with a speed of 20rpm. This is due to the fact

that, for the same flow rate, the filling of the screw decreases when the speed increases, causing the pressure exerted by the water on the blades of the screw to decrease.

6.1. Efficiencies

The efficiencies obtained are graphically summarized in the figure below, confronted with the flow rate:

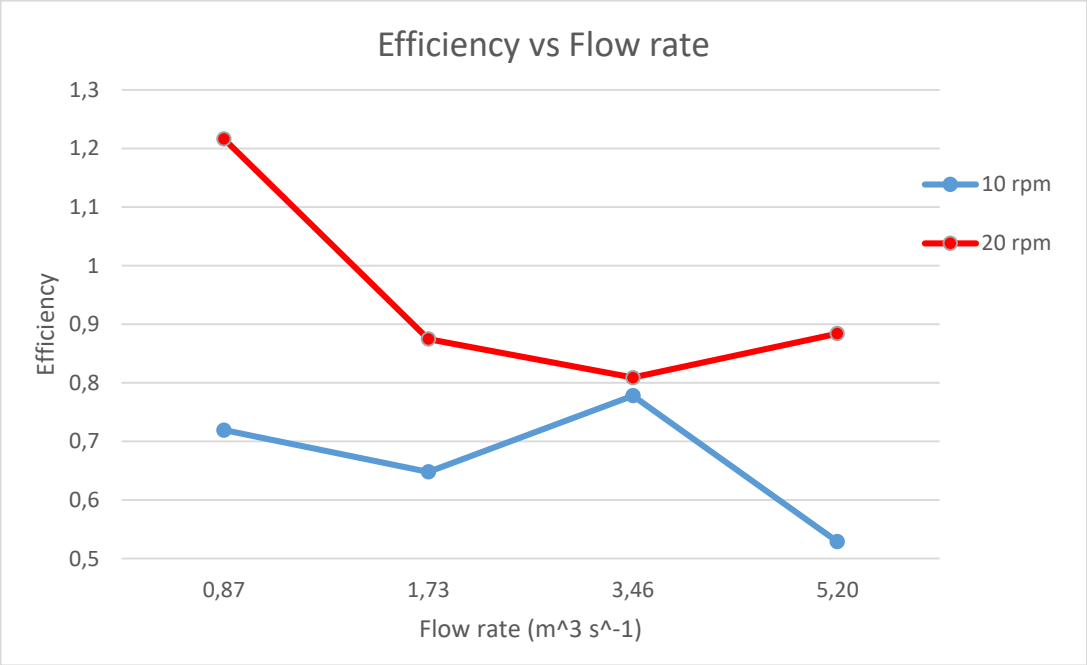

Figure 6.1 Efficiency vs. Flow rate

The point that stands out most is the efficiency generated by the screw when it turns at a speed of 20 rpm and with a flow of 0.87 $m^3 s^{-1}$. This efficiency is greater than one, in other words, the mechanical power generated by the screw is greater than the hydraulic power of the water. This means that the screw rotates faster than the force of the water would cause, and never fills the screw so that it rotates at that speed. It can be seen as with the same flow rate but with half of the rotation speed, the screw gets a considerably high efficiency, of 72%.

In the previous diagram (Figure 6.1), it can be seen how the simulation of 10 rpm and a flow of 5.20 $m^3 s^{-1}$, the efficiency has been really very low compared to other efficiencies. This may be because the screw rotates at a very slow rotation speed and a large flow rate enters, causing a very fast filling of the screw and, consequently, that this works in over-filling.

In general, generator efficiencies are higher when the screw rotates at 20 rpm, with a minimum flow rate of 1.73 $m^3 s^{-1}$, although the efficiencies given by the screw turning at 10 rpm are

not bad at all. Except for the two cases mentioned previously, efficiencies range from 65% to 90%. This gives the understanding that the screw can work with a wide range of flow rates and giving a considerably high efficiency.

It can also be seen how the efficiencies with a flow of 3.46 $m^3 s^{-1}$ are very similar and both are considerably high. This may suggest that the optimal flow rate at which the screw should operate is close.

6.2. Temporal evolution of torque

As for the temporal evolution of the screw torque, it can be seen in the following figure (Figure 6.2) that there is a periodic evolution in its maximum and minimum. These extremes are separated by a second of difference. That's how long it takes for a blade to make a third turn, and therefore, the screw makes a turn in three seconds. In these three seconds there are three torque peaks, the same number of blades that the screw has. As it can be seen, the fluctuations of the torque are not insignificant, and therefore not negligible. This is because the outer radius of the screw and its length are in the same order of magnitude. If these fluctuations are to be reduced, the length of the screw or the number of screw blades should be increased.

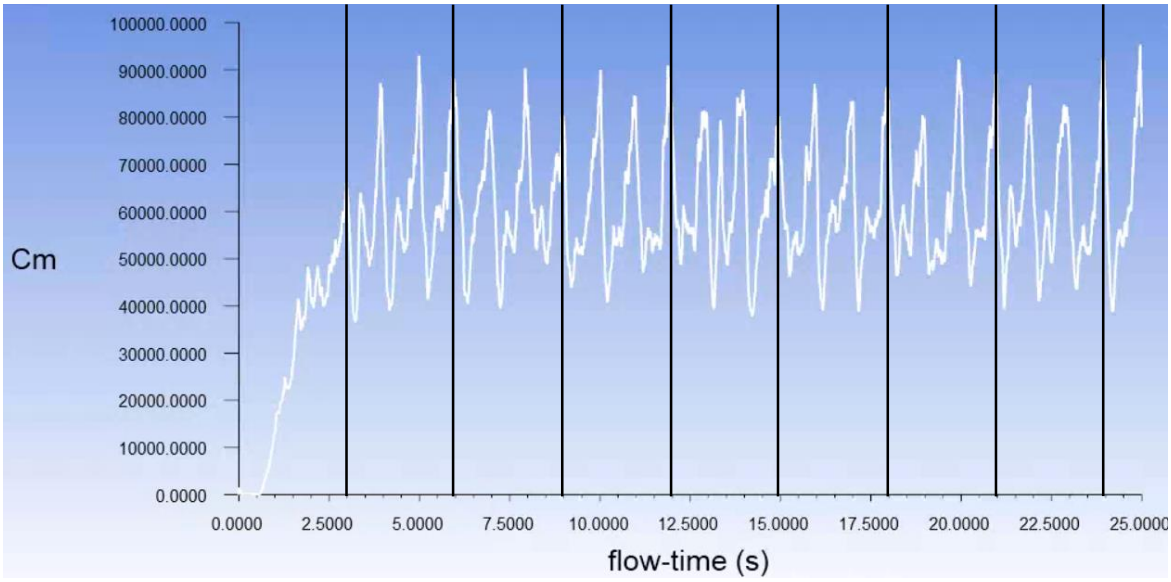

Figure 6.2 Temporal evolution of the torque for 20 rpm and 5.20 $m^3 s^{-1}$

It can be seen in the following figure (Figure 6.3) that at a much lower flow rate, the torque fluctuations are much smaller than at a higher flow rate, as in the previous case. In this case, the screw turns at 10 rpm, that is, the screw makes one revolution every 6 seconds. In this time interval, it can be observed that there are no very marked torque peaks, in other words, the torque is more constant than in the previous case. This is due to the fact that since the flow rate is not so large, the torque

variation is much smaller than in large flow rates, because the water does not hit the screw blades as hard as in larger flows.

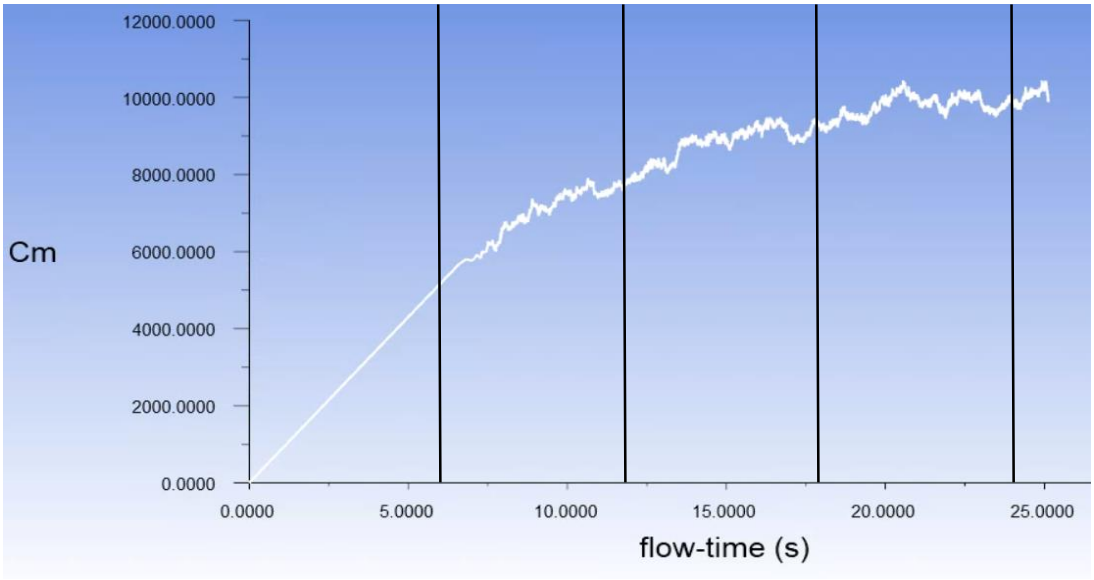

Figure 6.3 Temporal evolution of the torque for 10 rpm and 0.87 $m^3 s^{-1}$

6.3. Flow visualization

In the following figure (Figure 6.4), it is possible to visualize the water free surface present in the screw in the second 25 of simulation, with a rotation speed of 10rpm and a flow rate of 0.87 m^3s^{-1}. It can be seen how a big part of the water leaks through the gap between the screw blades and the trough.

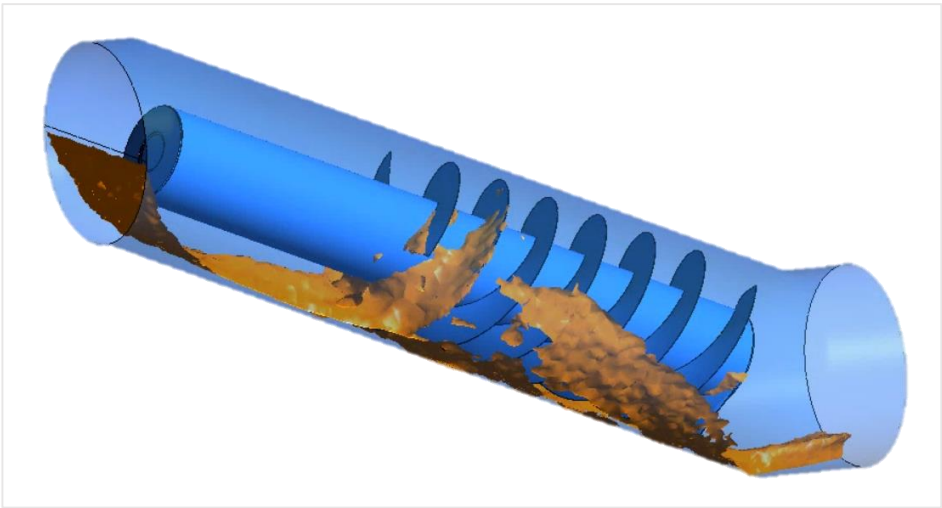

Figure 6.4 Visualization of water free surface with 10 rpm and 0.87 $m^3 s^{-1}$ in the second 25 of simulation

As the velocity inlet of the water is low, the filling of the screw is very slow and this causes the water to escape through the gap. This may be one of the reasons why the efficiency of this simulation is 72%, which speaking of this type of generators, is considered low. Apart from the leakage losses, another reason why the screw does not fill up completely, is that the inlet flow is not very high. With higher flow rates, concretely with a flow rate four times greater, the efficiency increases considerably, and that may be because the screw fills up more. The problem of leakage losses could have been reduced when creating the geometry for the simulation, specifically when the negative was extracted from the geometry, reducing the size of the trough and thus making the gap smaller.

7. Conclusions

CFD simulations are becoming very important to better understand the behaviour of fluids around complex geometries for different boundary conditions. It is very important to keep in mind that this tool has to be only a complement and an aid tool to understand the behaviour of the fluids, and always has to be accompanied by experimental measurements.

The main objective of this thesis was to successfully perform a simulation of an Archimedes screw operating as an electric generator. The objective has been more than fulfilled, as several simulations have been carried out and the results obtained have been physically logical. In this thesis, the simulations have been performed with the Ansys Fluent software, solving Reynolds averaged Navier-Stokes equations with the k-ω SST turbulence model. As this is a multiphase problem, with two different fluids such as water and air, the Volume of Fraction (VoF) method has been used to solve the problem of free surface position. To successfully simulate the screw rotation, a dynamic mesh was used with the smoothing and remeshing methods.

This work has been carried out with the aim that in the future, more simulations can be performed only by changing the boundary conditions in an easy way, and that these simulations can be compared with results obtained experimentally through tests made in a laboratory with the physical turbine as such.

The Archimedes screw demonstrates great efficiencies for the generation of hydraulic electricity in low head sites, but it is still a very new technology and needs to be well researched to get the most out of its potential. The efficiencies obtained in this thesis are really high when the screw rotates at a low rotation speed and with not very large inlet flow rates, but they could be better considering that they tend to show very high efficiencies, better than the ones obtained in the simulations.

Regarding the temporal evolution of the screw torque, this factor is found in most hydraulic turbines, and it is important to know this and take it into account when designing the screw and deciding how many blades the screw has to have as it can affect the production of energy.

As far as the visualization of the flow is concerned, the gap between the blades of the screw and the trough could have been reduced when extracting the negative from the geometry, in this way water would not escape through this gap, reducing leakage losses. Thus, perhaps even more satisfactory results would have been obtained.

In order to achieve optimal screw design, many more such simulations should be performed in order to obtain as much data as possible for comparison with experimental data. In this thesis only eight simulations have been made because each simulation takes a lot of computational time, but in

the future it would be good to make more and with the changes mentioned above, as well as changes of screw inclination, different flows and different rotation speeds, in order to obtain more varied and accurate results. The results obtained in this thesis should be of help for the design of the Archimedean screw, although some computational simulations always have to be accompanied by experimental measurements.

References

[1] J. Elcacho, “Las renovables producen el 100% de la electricidad de Alemania, por unas horas,” 03 May 2018. [Online]. Available: https://www.lavanguardia.com/. [Accessed 13 January 2019].

[2] International Hydropower Association, “International Hydropower Association,” May 2017. [Online]. Available: https://www.hydropower.org/country-profiles/germany. [Accessed 27 December 2018].

[3] G. Dellinger, P.-A. Garambois, N. Dellinger, M. Dufresne, A. Terfous, J. Vazquez and A. Ghenaim, “Computational fluid dynamics modeling for the design of Archimedes Screw Generator,” in *Renewable Energy*, Elsevier, 2018, pp. 847-857.

[4] S. R. Waters, “Analysing the performance of the Archimedes screw turbine within tidal range technologies,” Lancaster, UK, 2015.

[5] R. Lewis, “A composite bulk molding compound prevents wear and downtime,” Zeon Technologies Inc., April 2013. [Online]. Available: https://www.pumpsandsystems.com/topics/pumps/centrifugal-pumps/molding-resin-improve-wear-resistance. [Accessed 24 October 2018].

[6] KSB, “Centrifugal Pump Lexicon,” KSB SE & CO., [Online]. Available: https://www.ksb.com/centrifugal-pump-lexicon/archimedean-screw-pump/191708/. [Accessed 27 October 2018].

[7] S. Simmons, “A computational fluid dynamic analysis of Archimedes screw generators,” Guelph, Ontario, Canada, 2018.

[8] V. Oudendijk, Director, *Archimedean Screw Turbines: How it works.* [Film]. Lex de Prieëlle & Johnny Roek, 2012.

[9] A. Stergiopoulou and E. Kalkani, “Investigating the hydrodynamic behaviour of innovate Archimedean hydropower turbines,” Athens, 2013.

[10] J. Rohmer, D. Knittel , G. Sturtzer, D. Flieller and J. Renaud, “Modeling and experimental results of an Archimedes screw turbine,” in *Renewable Energy*, Elsevier, 2016, pp. 136-146.

[11] J. F. Wendt, J. D. Anderson Jr, J. Degroote, G. Degrez, E. Dick, R. Grundmann and J. Vierendeels, Computational fluid dynamics, Rhode-Saint-Genèse: Springer, 2009.

[12] NASA, "X-43A Hyper-X Photo Collection," NASA, 1997. [Online]. Available: https://www.dfrc.nasa.gov/Gallery/Photo/X-43A/Large/ED97-43968-1.jpg. [Accessed 21 December 2018].

[13] Z. Zhang and Q. Chen, "Comparison of the Eulerian and Lagrangian methods for predicting particle transport in enclosed spaces," in *Atmospheric Environment*, Elsevier, 2007, pp. 5236-5248.

[14] P. R. Spalart and S. R. Allmaras, "A one-equation turbulence model for aerodynamics flows," 1994.

[15] Fluent Inc, "Spallart-Allmaras model theory," Ansys Inc., 20 September 2006. [Online]. Available: https://www.sharcnet.ca/Software/Fluent6/html/ug/node469.htm. [Accessed 15 January 2019].

[16] Fluent Inc., "Standard k-epsilon model," Ansys Inc., 20 September 2006. [Online]. Available: https://www.sharcnet.ca/Software/Fluent6/html/ug/node478.htm. [Accessed 15 January 2019].

[17] M. Pavlovich Bulat and P. Victorovich Bulat, "Comparison of Turbulence Models in the Calculation of Supersonic Separated Flows," in *World Applied Sciences Journal*, Saint-Petersburg, IDOSI Publications, 2013, pp. 1263-1266.

[18] F. R. Menter, "Zonal Two Equation k-w Turbulence Models for Aerodynamic Flows," AIAA, Sunnyvale, CA, 1993.

[19] Fluent Inc., "RNG k-epsilon model," Ansys Inc., 20 September 2006. [Online]. Available: https://www.sharcnet.ca/Software/Fluent6/html/ug/node479.htm. [Accessed 15 January 2019].

[20] Fluent Inc., "Realizable k-epsilon model," Fluent Inc., 20 September 2006. [Online]. Available: https://www.sharcnet.ca/Software/Fluent6/html/ug/node480.htm. [Accessed 16 January 2019].

[21] Fluent Inc., “Standard k-omega model,” Ansys Fluent, 20 September 2006. [Online]. Available: https://www.sharcnet.ca/Software/Fluent6/html/ug/node486.htm. [Accessed 16 January 2019].

[22] Fluent Inc., “Shear-Stress Transport (SST) k-omega model,” Ansys Inc., 20 September 2006. [Online]. Available: https://www.sharcnet.ca/Software/Fluent6/html/ug/node487.htm. [Accessed 18 January 2019].

[23] J.-M. Hervouet, Hydrodynamics of Free Surface Flows: Modelling with the Finite Element Method, Chichester: John Wiley & Sons, Ltd, 2007.

[24] F. S. Inc., “FLOW-3D,” Flow-3D, [Online]. Available: https://www.flow3d.com/resources/cfd-101/general-cfd/free-surface-modeling-methods/. [Accessed 18 January 2019].

[25] M. I. Uddin and M. M. Karim, “Application of Volume Of Fluid (VOF) Method for Prediction of,” in *Procedia Engineering*, Elsevier, 2017, pp. 82-89.

[26] Ansys Inc., “Computational Fluid Dynamics Solution,” Canonsburg, PA, 2005.

[27] G. Dellinger, P.-A. Garambois, M. Dufresne, A. Terfous, J. Vazquez and A. Ghenaim, “Numerical and experimental study of an Archimedes Screw Generator,” in *IOP Conference Series: Earth and Environment Science (EES)*, Bangkok, IOP Publishing Ltd, 2016.

8. Appendix

The configuration of the simulations with Ansys was carried out following the following steps. First, the geometry was imported into Ansys Workbench DesignModeler, where a partition of the face of the fluid inlet was made, trying to simulate the flow of a river. This was followed by Ansys Meshing.

The mesh was constructed with an element size of 0.0675 m. It was very important to name the different parts of the geometry in order to configure the simulation correctly. The necessary parts were the following:

- The screw as such

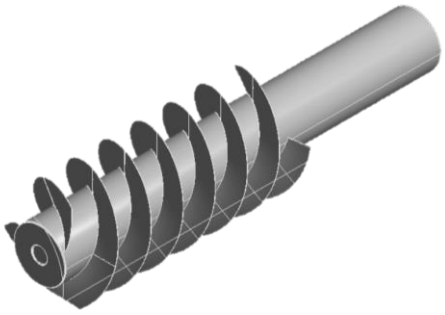

Figure 8.1 Screw

- The walls of the trough

Figure 8.2 Wall

- The outlet

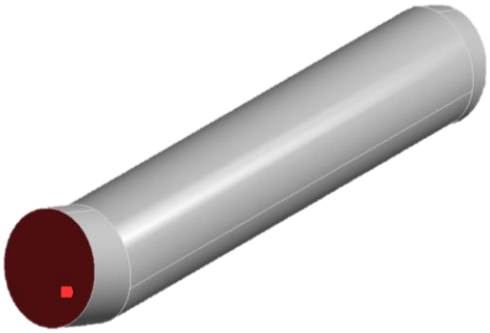

Figure 8.3 Outlet

- The inlet of the water

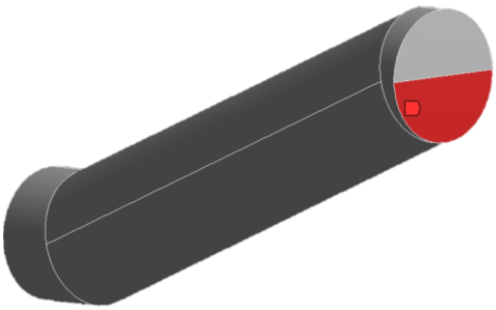

Figure 8.4 Water inlet

After this, the simulation could already be configured with Ansys Fluent. A transient simulation was set up, as shown in the following figure. Gravity was configured as can be seen in the image below (Figure 8.5) because the axes of the geometry are inclined to give the inclination to the screw. In the tree diagram of the image (Figure 8.5), the steps that have been followed to configure the simulation can be seen. In this section it is important to check the mesh to make sure that Fluent has detected all parts of the mesh in question.

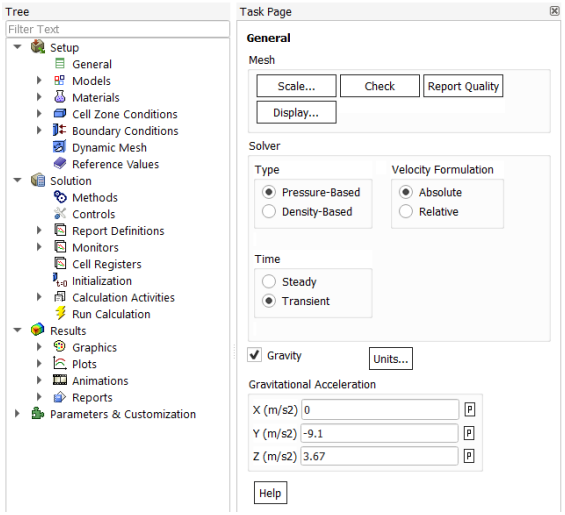

Figure 8.5 Transient simulation and gravity configuration

The next step was to configure the turbulence model to solve the RANS equations, which in this case was the k-omega SST model. The free surface flow model was also configured, which was the Volume of Fluid (VoF) model.

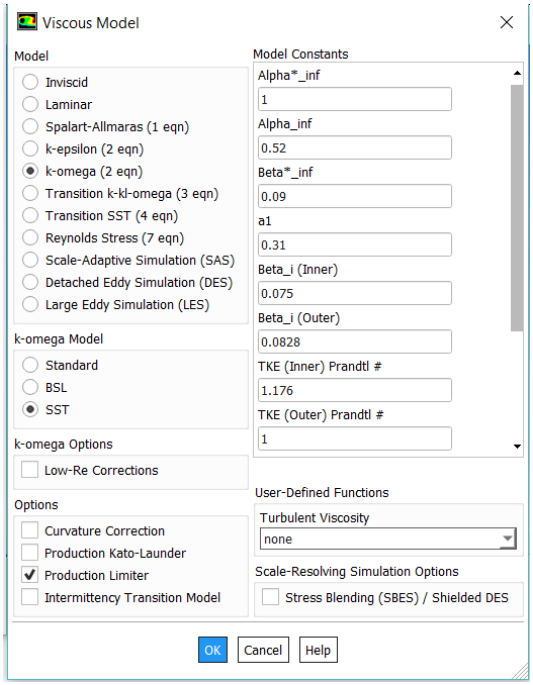

Figure 8.6 Viscous model

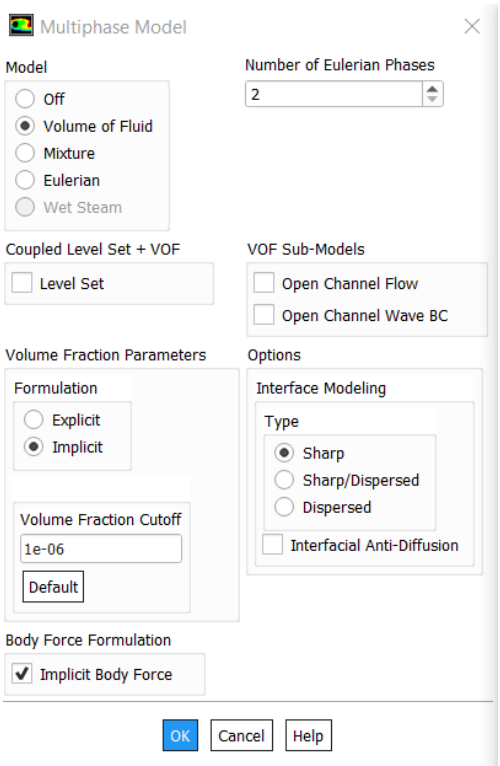

Figure 8.7 Multiphase model

The next thing to do was to define the two phases that were going to be present in the simulation and the interaction between them. These two phases were air and water.

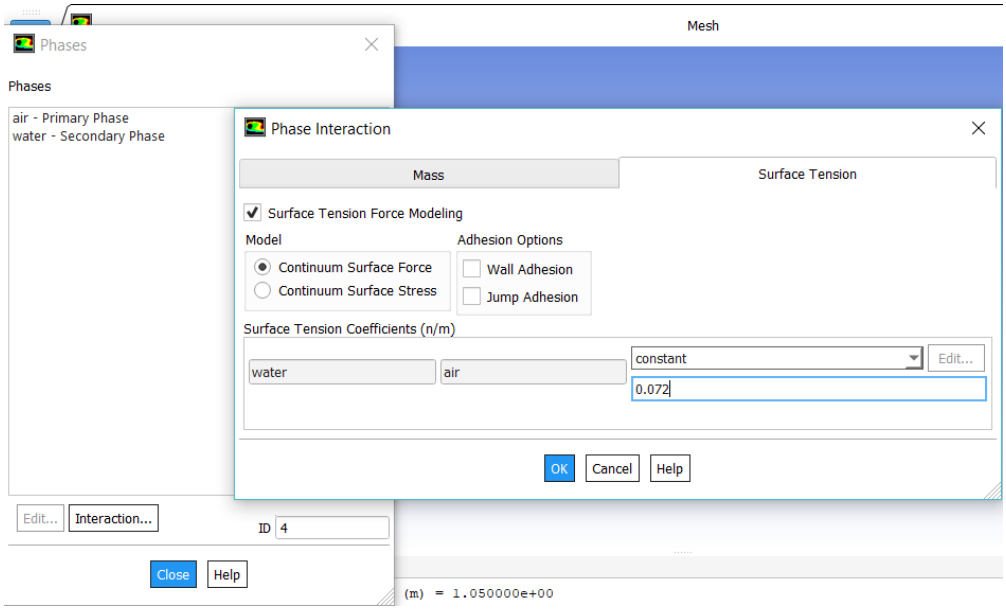

Figure 8.8 Phases and their interaction

Next, it was necessary to configure the velocity at which water entered the domain, and this velocity depended on the simulation being carried out. The value of this velocity ranged between 0.5 and 3 m s^{-1}.

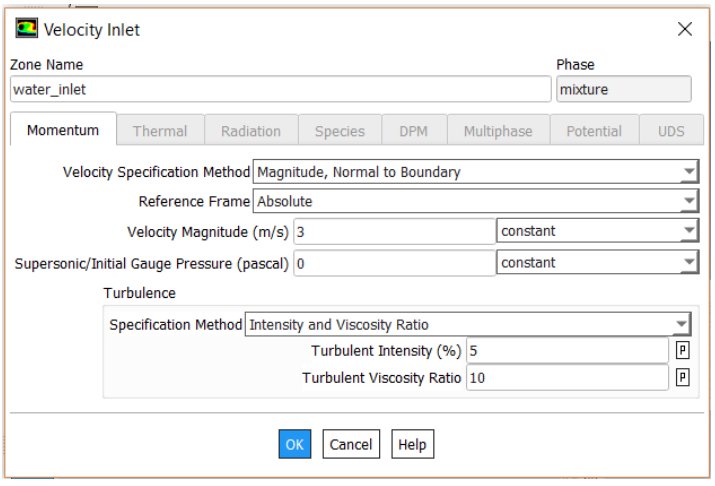

Figure 8.9 Velocity inlet

It was necessary to introduce an air inlet so that, initially, the screw would be filled with air and not water. To do this, Ansys Fluent detected the semicircle above the water inlet as a wall. This was changed to an air inlet at a very low speed so that this inlet did not affect the result of the torque. In this same section, the phase in which the flow of fluid entered the domain, which in this case was water, was defined. Therefore, the volume fraction was equal to 1.

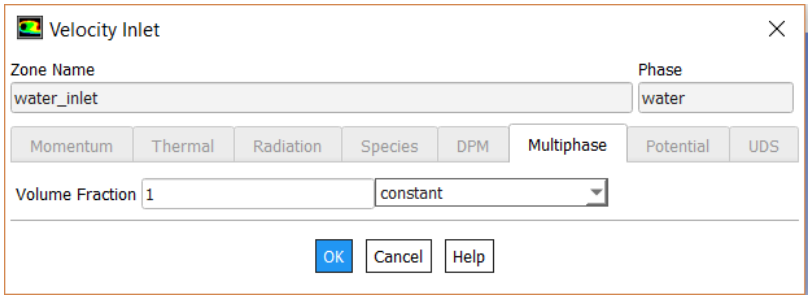

Figure 8.10 Volume fraction

The next step was to configure the dynamic mesh. To do this, a UDF file had to be previously loaded. This UDF file is used to define the rotation speed of the screw through a code thus simplifying the calculation of Fluent. The code can be seen in the image below. The rotational speed was defined according to each simulation, in rad s^{-1}.

```
#include "udf.h"
#include "math.h"
#include "dynamesh_tools.h"

DEFINE_CG_MOTION(rotation_udf, dt, vel, omega, time, dtime)
{
        NV_S (omega, =, 0.0);

        omega[2]=-1.05;
}
```

Figure 8.11 UDF code

Once this file was compiled, the dynamic zone was defined. This zone was the screw itself, the zone previously defined in the mesh. To do this, the UDF file was selected to define the rotation of the screw, the center of gravity of the screw was introduced and a maximum cell height equal to the size of the mesh element was introduced, as can be seen in the following images.

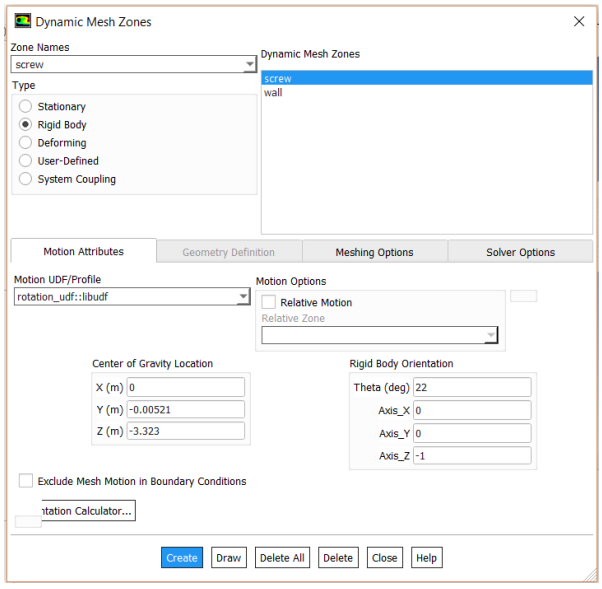

Figure 8.12 Dynamic mesh of the screw 1

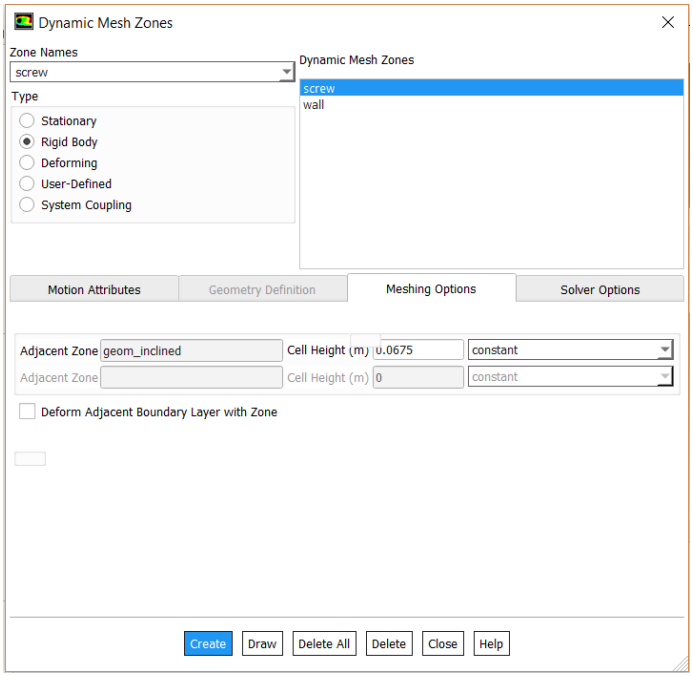

Figure 8.13 Dynamic mesh of the screw 2

In the same window, once the movement of the screw was defined, the wall zone was defined as stationary, in order to avoid the movement of this zone.

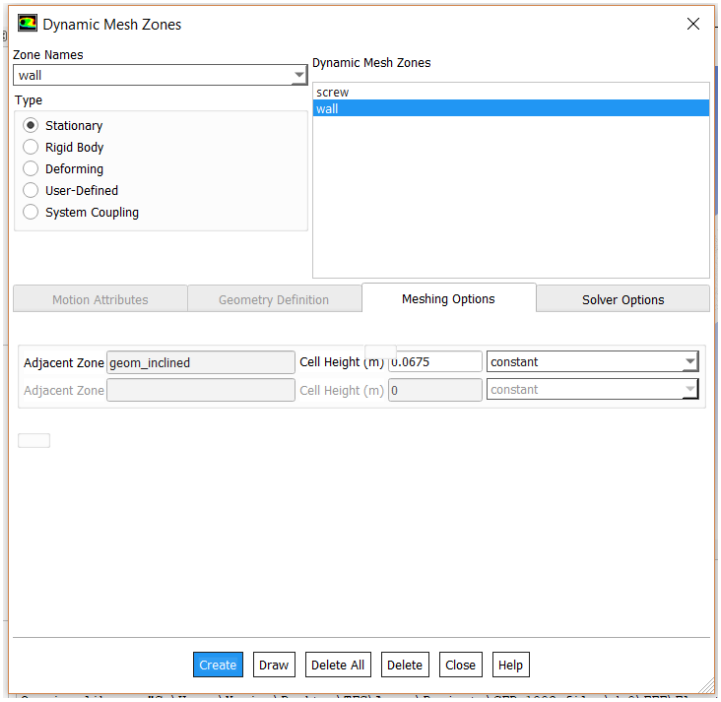

Figure 8.14 Dynamic mesh of the wall

Once the two zones of the dynamic mesh were defined, the settings of the dynamic mesh had to be defined. The mesh would be modified with the smoothing and remeshing methods. To do this, these two methods would be adjusted to the existing mesh as shown in the following image (Figure 8.15).

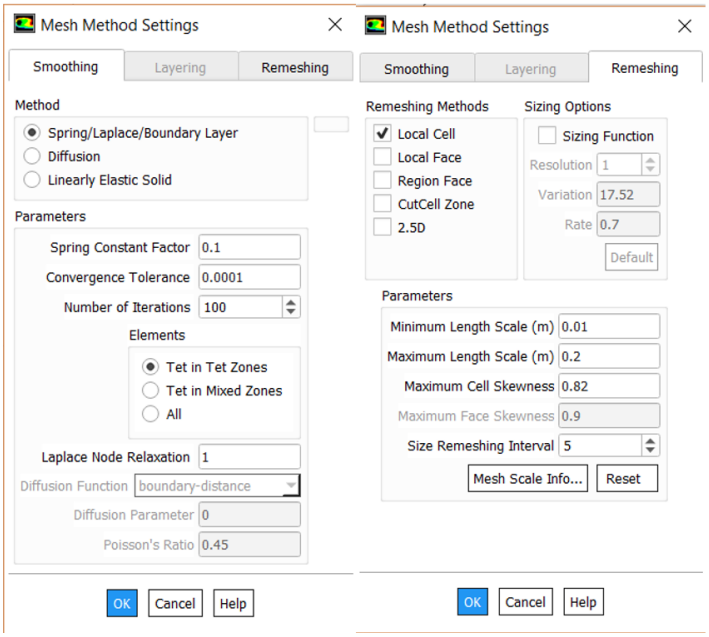

Figure 8.15 Smoothing and remeshing settings

With all this configured, the initialization of the solution was done with a hybrid initialization.

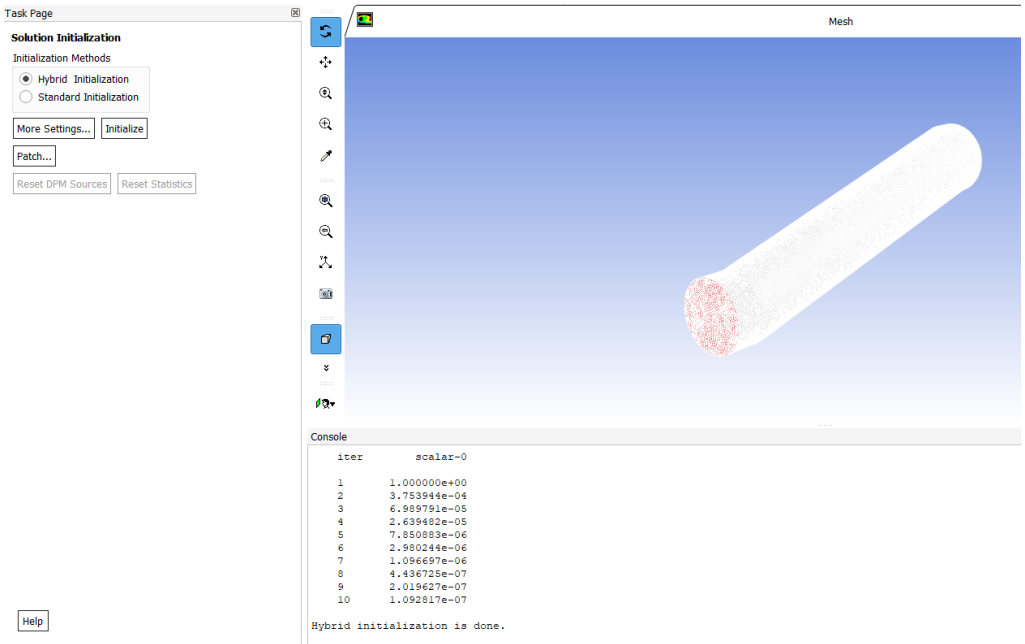

Figure 8.16 Hybrid Initalization

To start the simulation, a Time Step Size of 0.005 seconds was set, in order to obtain an accurate simulation according to reality. To obtain a long and truthful simulation, a number of Time Steps of 5000 was configured, with 25 iterations in each Time Step, and finally calculate.

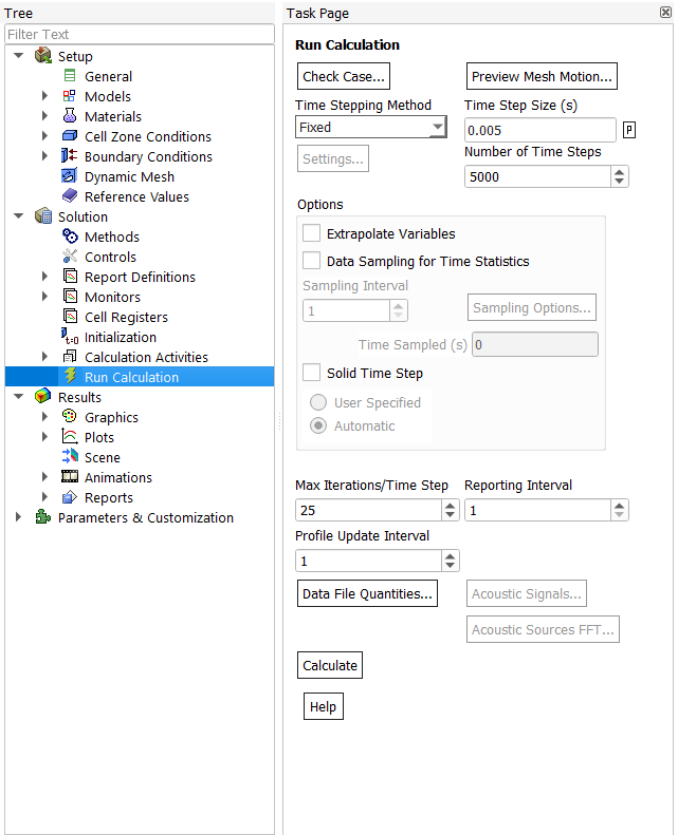

Figure 8.17 Final step